Published in final edited form as:
J Am Chem Soc. 2008 October 29; 130(43): 14189–14200. doi:10.1021/ja8031828.

Rational Tuning of the Thiolate Donor in Model Complexes of Superoxide Reductase: Direct Evidence for a Trans Influence in Fe^{III}-OOR Complexes

Frances Namuswe[†], **Gary D. Kasper**[†], **Amy A. Narducci Sarjeant**[†], **Takahiro Hayashi**[‡], **Courtney M. Krest**[§], **Michael T. Green**[§], **Pierre Moënne-Loccoz**[*,‡], and **David P. Goldberg**[*,†]

[†]Department of Chemistry, Johns Hopkins University, Baltimore, Maryland 21218

[‡]Department of Environmental and Biomolecular Systems, OGI School of Science and Engineering, Oregon Health & Science University, Beaverton, Oregon 97006

[§]Department of Chemistry, Pennsylvania State University, University Park, Pennsylvania 16802

Abstract

Iron peroxide species have been identified as important intermediates in a number of non-heme iron as well as heme-containing enzymes, yet there are only a few examples of such species either synthetic or biological that have been well characterized. We describe the synthesis and structural characterization of a new series of five-coordinate (N_4S(thiolate))Fe^{II} complexes that react with *tert*-butyl hydroperoxide (tBuOOH) or cumenyl hydroperoxide (CmOOH) to give metastable alkylperoxo-iron(III) species (N_4S(thiolate)Fe^{III}-OOR) at low temperature. These complexes were designed specifically to mimic the non-heme iron active site of superoxide reductase, which contains a five-coordinate iron(II) center bound by one Cys and four His residues in the active form of the protein. The structures of the Fe^{II} complexes are analyzed by X-ray crystallography, and their electrochemical properties are assessed by cyclic voltammetry. For the Fe^{III}-OOR species, low-temperature UV-vis spectra reveal intense peaks between 500 – 550 nm that are typical of peroxide to iron(III) ligand-to-metal charge-transfer (LMCT) transitions, and EPR spectroscopy shows that these alkylperoxo species are all low-spin iron(III) complexes. Identification of the vibrational modes of the Fe^{III}-OOR unit comes from resonance Raman (RR) spectroscopy, which shows ν(Fe-O) modes between 600 – 635 cm^{-1} and ν(O-O) bands near 800 cm^{-1}. These Fe-O stretching frequencies are significantly lower than those found in other low-spin Fe^{III}-OOR complexes. Trends in the data conclusively show that this weakening of the Fe-O bond arises from a *trans* influence of the thiolate donor, and DFT calculations support these findings. These results suggest a role for the cysteine ligand in SOR, and are discussed in light of the recent assessments of the function of the cysteine ligand in this enzyme.

Introduction

Iron peroxide species are proposed to play important roles in the function of many mononuclear iron centers in biology, including heme systems such as cytochrome P450[1–6] and heme oxygenase,[7] and non-heme iron centers such as bleomycin,[8–10] extradiol[10–13]and Rieske dioxygenases,[10,11] and superoxide reductases.[14–19] The latter enzymes represent a new class

---

ploccoz@ebs.ogi.edu; dpg@jhu.edu.

Supporting Information Available: X-ray structure files for **2, 3, 4** and **5** (CIF). UV-vis spectra of the titration of [Fe^{II}([15]aneN_4)(SPh)(BF_4)] with ^{t}BuOOH. Resonance Raman spectra of [Fe^{III}([15]aneN_4)(SAr)($^{18}O^{18}O^{t}Bu$)]$^+$ and [Fe^{III}([15]aneN_4)(SAr)($^{18}O^{18}OCm$)]$^+$ complexes. Complete ref 56. This material is available free of charge via the Internet at http://pubs.acs.org.

of iron-containing proteins that is found in anaerobic and microaerophilic prokaryotes, and catalyzes the reduction of superoxide to hydrogen peroxide through a reductive pathway, $O_2^- + e^- + 2H^+ \rightarrow H_2O_2$. SOR is thought to serve as an alternative to the classical superoxide dismutases (SODs), allowing anoxic microorganisms to avoid the oxidative half-reaction of SOD, which would produce deleterious dioxygen. The metal center in SOR that carries out the reduction of O_2^- is comprised of an Fe^{II} ion bound to the protein by four His donors in a plane and a single axial cysteinate donor, completing a square pyramidal geometry for the high-spin ferrous (reduced) enzyme. High-resolution X-ray structures of SOR have also shown that the Cys sulfur atom is within hydrogen-bonding distance of two N-H amide groups (N-H---S bonds) from the peptide backbone.[20] The mechanism of O_2^- reduction has been studied by several methods, and there is one intermediate, characterized by an absorption band at ~600 nm,[16,17,19,21] that has been consistently observed. This species has been formulated as an iron (III)-(hydro)peroxo species. However, the structure, spin state, and protonation state of this intermediate have not been definitively determined, and the possible existence of other iron peroxide-type intermediates along the catalytic pathway remains under investigation. In addition, the thiolate ligand in SOR is unique among non-heme iron enzymes, and its role in the mechanism of O_2^- reduction has been a subject of much interest.[18,20,22,23]

We previously reported the synthesis of the SOR model complex $[Fe^{II}([15]aneN_4)(SC_6H_5)]^+BF_4^-$, and showed that it reacted with alkylhydroperoxides at low temperature in CH_2Cl_2 to give the metastable iron(III)-alkylperoxo species $[Fe^{III}([15]aneN_4)(SC_6H_5)(OOR)]^+$ (R = cumenyl or *tert*-butyl).[24] These complexes were characterized by UV-vis, EPR, and resonance Raman (RR) spectroscopies, and determined to be low-spin Fe^{III}-OOR species with weak Fe-O bonds, i.e., with ν(Fe-O) ~ 90 cm^{-1} lower than in other low-spin Fe^{III}-OOR species. Analysis of other low-spin and high-spin Fe^{III}-OO(H or R) species by RR spectroscopy has led to a trend in which the low-spin complexes exhibit strong Fe-O and weak O-O bonds, while the opposite trend is observed for the high-spin species.[25–32] Thus the $[Fe^{III}([15]aneN_4)(SC_6H_5)(OOR)]^+$ complexes were the first examples of low-spin Fe^{III}-OOR species to exhibit dramatically weakened Fe-O bonds. The former trend was used as precedent for the suggestion that the spin-state of the iron during O_2^- reduction may play a part in encouraging Fe-O bond cleavage and release of H_2O_2 as opposed to the O-O cleavage pathway observed for other enzymes such as cytochrome P450.[16,33–35]

In our earlier report we reasoned that the unexpected weakening of the Fe-O bond in $[Fe^{III}([15]aneN_4)(SC_6H_5)(OOR)]^+$ may arise from a *trans* influence of the thiolate donor, provided that the thiolate ligand was indeed coordinated in a *trans* configuration. Immediately following this work a report from Kovacs and Solomon[36] described the low-temperature synthesis and characterization of a *high-spin* Fe^{III}-OOH model of SOR that also exhibited a significantly weakened Fe-O bond, as evident from the RR-detected Fe-O stretch for this complex (ν(Fe-O) = 419 cm^{-1} versus 450–639 cm^{-1} for other high-spin iron(III) peroxides). In this study a thiolate-induced trans influence was also invoked as the potential cause of the weak Fe-O bond. In contrast, an earlier report by Que and Halfen[33] showed that increasing the electron-donating ability of a trans-oriented axial ligand (X) in a series of six-coordinate, high-spin $[Fe^{III}(N_4)(X)(OOR)]^+$ complexes led to a decrease in the decay rate of these species. This trend is opposite to that expected for a weakening of the Fe-O bond via a trans influence of X, assuming that the decay involves Fe-O bond cleavage. Interestingly, the RR spectroscopy on these high-spin complexes displayed essentially no variance with the identity of the axial ligand. We speculated that the synthesis of a series of SOR models in which the electron-donating power of the thiolate ligand was rationally varied would greatly aid in determining the potential role of this ligand in influencing the properties of Fe-OO(H or R) species.

In this paper, we describe the modular synthesis of a series of SOR model complexes of the type $[Fe^{II}([15]aneN_4)(SAr)]^+$, wherein the thiolate ligand has been varied with regard to its electron-donating ability. These complexes have allowed us to systematically assess the influence of the thiolate donor on the structural and physical properties, as well as the reactivity of this family of SOR model complexes while holding the remaining ligand set constant. The ability of these complexes to form Fe^{III}-OOR species is evaluated, and a mechanism of formation is proposed. The UV-vis features, spin-states and vibrational signatures of the Fe^{III}-OOR species are determined by low-temperature electronic absorption, EPR, and RR spectroscopies. The influence of the thiolate donor on the Fe-O and O-O bond strengths is assessed. DFT calculations were performed in support of the spectroscopic data. These findings are discussed in light of recent results on SOR in which the influence of the Cys donor on the properties of an Fe^{III}-OO(H) intermediate has been investigated through site-directed mutagenesis.[18]

Experimental Section

General Procedures

All reactions were carried out under an atmosphere of N_2 or Ar using a drybox or standard Schlenk techniques. 1,4,8,1 2-tetraazocyclopentadecane ([15]aneN_4) (98%) was purchased from Strem Chemicals. All other reagents were purchased from commercial vendors and used without further purification unless noted otherwise. Diethyl ether and dichloromethane were purified via a Pure-Solv Solvent Purification System from Innovative Technology, Inc. THF was distilled from sodium/benzophenone. Methanol was distilled over CaH_2. All solvents were degassed by repeated cycles of freeze-pump-thaw and then stored in a drybox. Sodium hydride (60% in mineral oil) was washed with hexanes prior to use. *Tert*-butylhydroperoxide was purchased from Aldrich as an ~5.5 M solution in decane over molecular sieves. The concentration of tBuOOH was measured via titration with potassium iodide according to a published procedure.[37] $^{t}Bu^{18}O^{18}OH$ was synthesized by the reaction of $^{t}BuMgCl$ with $^{18}O_2$ following a published procedure.[38] Cumene$^{18}O^{18}OH$ was synthesized by the reaction of cumene with $^{18}O_2$ following a published procedure.[39] $^{18}O_2$ was purchased from Icon Isotopes (99% atom purity).

Physical Methods

Electron paramagnetic resonance (EPR) spectra were obtained on a Bruker EMX EPR spectrometer controlled with a Bruker ER 041 X G microwave bridge at 15 K. The EPR spectrometer was equipped with a continuous-flow liquid He cryostat and an ITC503 temperature controller made by Oxford Instruments, Inc. Low-temperature UV-visible spectra were recorded at −78 °C on a Cary 50 Bio spectrophotometer equipped with a fiber-optic coupler (Varian) and a fiber optic dip probe (Hellma 661.302-QX-UV, 2 mm path length) for low temperature, using custom-made schlenk tubes designed for the fiber-optic dip probe. Room temperature UV-vis spectra were recorded on a Hewlett-Packard 8453 diode array spectrophotometer. Resonance Raman spectra were obtained on a custom McPherson 2061/207 spectrometer equipped with a Princeton Instrument liquid-N_2 cooled CCD detector (LN-1100OB). The 514-nm excitation from an Ar laser (Innova 90, Coherent) was set at 50 mW and continuous spinning of the sample at 110 K was used to prevent adverse effect from the laser illumination. A Semrock RazorEdge filter was used to attenuate Rayleigh scattering. Sets of ~15 min accumulations were acquired at 4-cm^{-1} resolution. Frequencies calibrations were performed using aspirin and are accurate to ±1 cm^{-1}. Elemental analyses were performed by Atlantic Microlab Inc., Norcross, GA.

Synthesis of $[Fe^{II}([15]aneN_4)(SC_6H_5)]BF_4$ (1)

To a solution of $Fe(BF_4)_2{\bullet}6H_2O$ (0.395 g, 1.17 mmol) in MeOH (4 mL) was added a solution of [15]aneN_4 (0.250 g, 1.17 mmol) in MeOH (6 mL) dropwise, and stirred for 45 minutes resulting in a pale yellow solution. A methanolic solution of $NaSC_6H_5$ (0.185 g, 1.40 mmol) (prepared from addition of benzenethiol to NaH in THF) was added to the mixture and stirred overnight to give a pale green solution. Methanol was removed under vacuum to give a green solid, which was redissolved in CH_2Cl_2 and filtered through celite to give a green solution. Vapor diffusion of diethyl ether into this solution resulted in colorless prisms (which appear light blue when grown together in clusters) of **1** after a week. Yield: 0.295 g (57%); *Anal*. Calc. for $C_{17}H_{31}N_4SFeBF_4$: C, 43.80; H, 6.71; N, 12.01. Found: C, 43.34; H, 6.85; N, 12.08.

Synthesis of [Fe^{II}([15]aneN_4)(SC_6H_4-*p*-Cl)]BF_4 (2)

To a solution of $Fe(BF_4)_2$•$6H_2O$ (0.378 g, 1.12 mmol) in MeOH (3 mL) was added a solution of [15]aneN_4 (0.267 g, 1.25 mmol) in MeOH (4 mL) dropwise, and stirred for 45 minutes resulting in a pale yellow solution. A methanolic solution of $NaSC_6H_4$-*p*-Cl (0.236 g, 1.39 mmol) (prepared from addition of 4-chlorobenzenethiol to NaH in THF) was added to the mixture and stirred for 30 minutes to give a pale yellow solution. Methanol was removed under vacuum to give a yellow-brown solid, which was redissolved in CH_2Cl_2 and filtered through celite to give a forest green solution. Vapor diffusion of diethyl ether into this solution resulted in colorless prisms (which appear pale green when grown together in clusters) of **2** after 2 days. Yield: 362 mg (65%); *Anal*. Calc. for $C_{17}H_{30}N_4SFeClBF_4$: C, 40.78; H, 6.04; N, 11.09. Found: C, 40.79; H, 5.66; N, 11.33.

Synthesis of [Fe^{II}([15]aneN_4)(SC_6H_4-*p*-OMe)]BF_4 (3)

To a solution of $Fe(BF_4)_2$•$6H_2O$ (0.236 g, 0.700 mmol) in MeOH (4 mL) was added a solution of [15]aneN_4 (0.150 g, 0.700 mmol) in MeOH (6 mL) dropwise, and stirred for 45 minutes resulting in a pale yellow solution. A methanolic solution of $NaSC_6H_4$-*p*-OMe (prepared from the addition of 4-methoxybenzenethiol to NaH in THF) was added to the mixture and stirred overnight to give a pale green-yellow solution. Methanol was removed under vacuum to give a green solid, which was redissolved in CH_2Cl_2 and filtered through celite to give a yellow-green solution. Vapor diffusion of diethyl ether into this solution resulted in colorless rods (which appear pale green when grown together in clusters) of **3** after one week. Yield: 0.226 g (65%); *Anal*. Calc. for $C_{18}H_{33}N_4OSFeBF_4$: C, 43.57; H, 6.70; N, 11.29. Found: C, 43.51; H, 6.73; N, 11.31.

Synthesis of [Fe^{II}([15]aneN_4)(SC_6F_4-*p*-SC_6F_5]BF_4 (4)

To a solution of $Fe(BF_4)_2$•$6H_2O$ (0.284 g, 0.84 mmol) in MeOH (3 mL) was added a solution of [15]aneN_4 (0.180 g, 0.84 mmol) in MeOH (4 mL) dropwise, and stirred for 45 minutes resulting in a pale yellow solution. A methanolic solution of $NaSC_6F_4$-*p*-SC_6F_5 (0.266 g, 0.66 mmol) (4 mL) (prepared in situ from addition of 2,3,4,5,6-pentafluorobenzenethiol to NaH in THF) was added dropwise to give a dark yellow solution, which was stirred for 30 minutes. Methanol was removed under vacuum to give a dark yellow solid. The solid was dissolved in CH_2Cl_2 and filtered over celite to give a dark yellow solution. Vapor diffusion of diethyl ether into this solution resulted in colorless thick plates (which appear yellow when grown together in clusters) of **4** after 3 weeks. *Anal*. Calc. for $C_{23}H_{26}N_4S_2FeClBF_{13}$: C, 37.52; H, 3.56; N, 7.61. Found: C, 37.33; H, 3.49; N, 8.16.

Synthesis of [Fe^{II}([15]aneN_4)(SC_6H_4-*p*-NO_2)]BF_4 (5)

To a solution of $Fe(BF_4)_2$•$6H_2O$ (0.239 g, 0.707 mmol) in MeOH (3 mL) was added a solution of [15]aneN_4 (0.152 g, 0.707 mmol) in MeOH (4 mL) dropwise, and stirred for 45 minutes resulting in a pale yellow solution. A red solution of $NaSC_6H_5$-*p*-NO_2 (0.179 g, 1.01 mmol) in MeOH (4 mL) (prepared from the addition of 4-nitrobenzenethiol to NaH in THF) was added dropwise to give a dark red solution with orange-yellow precipitate, which was stirred for 30 minutes. The solvent was removed under vacuum to give a dark red solid interspersed with small amounts of an orange solid. The solid was dissolved in CH_2Cl_2 and filtered through celite to give a dark red solution. Vapor diffusion of diethyl ether into this solution resulted in dark red prisms of **5** after 1 day. Yield: 0.240 g (66%); UV-vis (CH_2Cl_2, 11463 $M^{-1}cm^{-1}$), λ_{max} 370 nm, 490 nm (sh); *Anal*. Calc. for $C_{17}H_{30}N_5SFeO_2BF_4$: C, 39.94; H, 5.92; N, 13.70. Found: C, 39.98; H, 5.96; N, 13.48.

X-ray crystallography

All X-ray diffraction data were collected on an Oxford Diffraction Xcalibur3 diffractometer, equipped with a Mo K-alpha sealed-tube source and a Sapphire CCD detector. Single crystals of each compound were mounted in oil under a nitrogen cold stream at 110(2) K. Data collection parameters are provided in supplementary information as CIF files. Selected crystallographic details are provided in Table 1. Data were collected, integrated, scaled and corrected for absorption using CrysAlis Pro software.[40] Structures were solved and refined using the SHELXTL suite of software.[41]

Disorder in structures comprising the [15]aneN_4 ligand is well documented.[42–55] The structures presented here were refined in non-centrosymmetric space groups in order to better model the disorder in the macrocycle. Elongated thermal parameters for the macrocycle atoms suggest that these atoms are significantly disordered. Attempts to further model this disorder did not improve the refinement. In structures **1**, **2**, **3** and **5**, the C-C and C-N bonds were restrained using values given by Blake, et al.[43] The hydrogen atoms were refined in calculated positions, using appropriate riding models. The atoms in the disordered C_6H_4-*p*-OMe and C_6H_4-*p*-NO_2 moieties of **3** and **5** respectively were refined isotropically. Complex **4**, which is rather well-ordered was refined with no distance restraints and all non-hydrogen atoms were refined anisotropically. The N-H hydrogen atoms were located from the residual electron density maps and freely refined, while all C-H hydrogen atoms were refined in calculated positions. For further details on all structures, see CIF files in supporting information.

Electrochemistry

Cyclic voltammograms were measured with an EG&G Princeton Applied Research potentiostat/galvanostat model 263A at scan rates of 0.025–0.5 V/s. A three-electrode configuration made up of a platinum working electrode, a Ag/AgCl reference electrode (3.5 M KCl), and a platinum wire auxiliary electrode was employed. Measurements were performed with 0.1 mM analyte in CH_2Cl_2 at ambient temperatures under argon using 0.10 M tetra-n-butylammonium hexafluorophosphate (recrystallized 3 times from ethanol/water, dried over high vacuum for 3 days and stored in the dry box) as the supporting electrolyte. The ferrocenium/ferrocene couple ($FeCp_2^{+/0}$) at 0.45 V was used as an external reference.

Computational Methods

Frequency calculations were performed at optimized geometries. Initial coordinates were taken from the X-ray crystal structures of the iron(II) complexes **1** – **5**. Calculations were performed with Gaussian 03 at the B3LYP/6–311G level of theory.[56] The potential energy distribution was obtained by transforming the calculated force constants and normal modes from Cartesian coordinates to an internal coordinate system.[57]

Generation of $[([15]aneN_4)Fe^{III}(SAr)(OOR)]^+$ for UV-vis spectroscopy

In a typical reaction, a custom-made schlenk flask was loaded with a known amount of $[Fe^{II}([15]aneN_4)$ (SAr)]BF_4 and dissolved in an appropriate volume of CH_2Cl_2 to give a final concentration of the Fe^{II} complex between 0.3 and 3 mM. A fiber optic dip probe with a path length of 2 mm was inserted into the flask under argon and the solution was cooled to −78 °C. After recording the UV-vis spectrum of the Fe^{II} starting material, 3 equivalents of tBuOOH (stock solution in *n*-decane) was diluted into CH_2Cl_2 and added to the Fe^{II} complex and a new spectrum was immediately recorded. The colorless solution instantly turned deep red except in the case of **5** where the light orange starting material gradually turned fuchsia. The formation and decay of the new species were followed by UV-vis spectroscopy.

Generation of $[Fe^{III}([15]aneN_4)(SAr)(OOR)]^+$ for Resonance Raman and EPR Spectroscopy

To a Wilmad WG-5M economy NMR tube or Wilmad Quartz EPR tube containing a known concentration of $[Fe^{II}([15]aneN_4)(SAr)]BF_4$ in CH_2Cl_2 (500 μL) cooled to −78 °C, was added 3 equivalents of ROOH (R = tBu or cumenyl) in CH_2Cl_2. An instant color change from colorless to deep red (light orange to fuchsia in the case of **5**) was observed, indicating the formation of the Fe^{III}-OOR species. The reaction mixture was then bubbled with Ar or N_2 gas in the EPR or NMR tube to obtain a homogenous solution. Bubbling was kept to a minimum in order to minimize warming of the solution. The solution was then frozen in liquid nitrogen and stored at 77 K until either RR or EPR measurements were made.

Results and Discussion

Synthesis

The iron(II) complexes **1** – **5** that form the basis of this study were prepared according to Scheme 1. The synthesis of complex **1** was communicated previously.[24] Reaction of $Fe(BF_4)_2$ with the tetraamine donor $[15]aneN_4$ in MeOH results in the insertion of Fe^{II} into the $[15]aneN_4$ cavity. A dark green color forms immediately upon addition of $[15]aneN_4$ to colorless $Fe^{II}(BF_4)_2$ in MeOH, which gradually fades to a pale yellow over the course of 45 minutes. The sodium salt of the appropriate arylthiolate ligand is then added, leading to the production of complexes **1** – **5**. Our initial synthesis involved changing the reaction solvent to CH_2Cl_2 before adding the thiolate ligand, but we have seen improved yields of the Fe^{II} complexes when adding ArS^-Na^+ in MeOH and then removing solvent. Recrystallization of **1** – **5** from CH_2Cl_2/Et_2O provided crystals for X-ray diffraction, and was the general method used for preparing pure **1** – **5** for all of the spectroscopic and reactivity studies described herein. Complexes **1** and **2** recrystallize as colorless prisms, complex **3** as colorless rods, while complex **4** recrystallizes as colorless thick plates. The sodium salt of $^-SC_6H_4$-*p*-NO_2 has an intense red color from an intraligand π-π* transition, which causes crystalline complex **5** to appear as dark red prisms.

The synthesis of these complexes is sensitive to the ratio of arylthiolate ligand versus iron(II). A slight excess of the thiolate ligand (1.25 – 2.0 equiv) compared to Fe^{II} is necessary to obtain these complexes in good yield and avoid other side-products. For example, when lower ratios of ArS^- are employed in the syntheses of **1** or **2**, a sideproduct appears as white needle-shaped crystals, easily discernable from crystalline **1** or **2** by visual inspection. The use of too large an excess of thiolate donor (three equivalents) in the case of the *p*-NO_2 complex **5** led to the formation of $[Fe^{II}([15]aneN_4)(SC_6H_4\text{-}p\text{-}NO_2)][SC_6H_4\text{-}p\text{-}NO_2]$, where the BF_4^- counterion has been replaced by a non-coordinating $^-SC_6H_4$-*p*-NO_2 ligand.[58] For the synthesis of polyfluorinated derivative **4**, the target complex was $[Fe^{II}([15]aneN_4)(SC_6F_5)]^+$, but nucleophilic displacement of the *p*-F substituent during the initial deprotonation of C_6F_5H with NaH led to the thioether-linked thiolate ligand shown in Scheme 1.

The modular synthetic approach taken in this study purposefully avoided covalently linking the thiolate donor to the N_4 ligand in order to allow for systematic variation of the electron-donating/releasing properties of the thiolate ligand. We were pleased to find that an extensive series of mononuclear, 5-coordinate iron(II) complexes could be assembled in this manner, provided that the thiolate-to-iron ratios are carefully controlled. Other iron(II) complexes with N_4S(thiolate) donor sets include $[Fe^{II}(L^8py_2)(SAr\ or\ SC_6H_{11})]BF_4$ (L^8py_2 = 1,5-Bis (pyridin-2-ylmethyl)-1,5-diazocane), which were prepared as models of SOR by a similar selfassembly approach,[59,60] and the covalently linked, thiolate-ligated complexes [Fe^{II}(cyclam-PrS)]BPh_4 and [Fe^{II}($S^{Me2}N_4$(tren))]PF_6 (tren = tris(2-aminoethyl)amine) from Kovacs and coworkers.[36,61,62] However, this study is the first report, to our knowledge, that allows for a direct assessment of the electronic influence of the thiolate donor at parity of ligand environment for a series of N_4S(thiolate)-iron complexes.

X-ray Structural Studies

The X-ray crystal structures of **2** – **5** are presented as ORTEP diagrams in Figure 1. Structural parameters are shown in Table 1, and selected bond lengths and angles for each complex are given in Table 2. The structure of **1** has been reported previously,[24] but is included in Table 1 and Table 2 for comparison. Each cationic iron(II) complex is five-coordinate, with four nitrogen donors from the [15]aneN_4 ligand and one sulfur donor from the ArS^- ligand completing the coordination sphere. The conformation for [15]aneN_4 is the same in each structure, with one N-H group (N(2)-H) on the same side of the macrocyclic plane as the thiolate ligand, while the other three N-H groups lie on the opposite side. The Fe–S bond distances for **1** – **5** range from 2.3197(12) – 2.3426(8) Å, showing little variance across the series and falling in the typical range for high-spin Fe^{II}-SR complexes.[63–66] For complexes **1** – **5**, the Fe-N distances range between 2.075(7) – 2.273(3) Å and are similar to other high-spin Fe(II) complexes, including the related N_4S(thiolate)Fe^{II} complex [Fe^{II}(Me_4cyclam)(SC_6H_4-*p*-OMe)]$^+$ (Fe-N = 2.183(6) – 2.279(6) Å).[60] For complexes **1** – **4** the Fe-N(3) distance (1: 2.138 (3); 2: 2.075(5) Å; 3: 2.095(8) Å; 4: 2.088(3) Å) is slightly shorter than the other three Fe-N bonds. These short distances may be a consequence of steric constraints imposed by the [15] aneN_4 ligand. The longest Fe-N distance in **1** – **4** is observed for N(2), which is also the only N-H group on the same side of the macrocycle as the sulfur donor. The *p*-nitro-benzenethiolate complex **5** exhibits Fe–N bond distances that are on the lower end of the range seen for **1** – **5**. These shorter distances may be a consequence of the weaker donation from the NO_2-substituted phenylthiolate ligand, which results in a more electropositive iron(II) center as evidenced by electrochemistry (vide infra). In addition, the NO_2 complex **5** exhibits a geometry closer to square pyramidal (sp) as determined by its τ value[67] of 0.27 (τ = 0.0 for idealized sp and 1.0 for idealized tbp) compared to τ ~0.5 for **1** – **4**, with its thiolate ligand occupying the axial position. A combination of the electron-poor nature of **5** along with this subtle geometry change may account for the shorter Fe-N distances in **5**.

The precise orientation of the thiolate donor in both metal-thiolate models and metalloproteins has been suggested to be important for controlling the sulfur-metal bonding interactions and related properties, including reduction potentials.[60,68,69] The orientation of the arylthiolate ligands in **1** – **5** can be defined by the Fe-S-C_{aryl} angle and Fe-S-C_{aryl}-C_{aryl}’ dihedral angle. The Fe-S-C_{aryl} angles for **1** – **5** are similar, lying between 109.7(6) – 116.90(12)°. The Fe-S-C_{aryl}-C_{aryl}’ dihedral angles are also similar for **1** – **3** and **5**, varying between 90.3(11) – 105.9 (8)°, while for the fluorinated complex **4** this angle is 132.8(2)°. Interestingly, the packing diagram of complex **4** shows a π-stacking interaction in the solid state between the C_6F_4 ring of one molecule and C_6F_5 ring of a neighboring molecule (X,1-Y, −½+Z), characterized by the following geometric parameters: Ct-Ct = 3.586 Å (Ct = centroid of the ring), α = 9.30° (α = dihedral angle between the stacking planes) and $D\perp$ = 3.296 Å and 3.403 Å ($D\perp$ = perpendicular distances from one ring to the plane of the other ring). This π-stacking interaction may be perturbing the Fe-S-C_{aryl}-C_{aryl}’ dihedral angle.

Comparison to the structure of the reduced enzyme, SOR_{red}

All of the model complexes **1** – **5** are five-coordinate iron(II) complexes with one open site on the metal, as found in SOR_{red}. The N_4S(thiolate) donor set of **1** – **5** is a good mimic of the coordination sphere of the iron(II) center in the active site. The Fe^{II}–S bond distances in **1** – **5**, which fall in the normal range, are somewhat shorter than that found in the enzyme (X-ray structure:[70] 2.40 – 2.44 Å; EXAFS:[71] 2.37 Å). It is not clear at present why SOR exhibits an elongated iron-sulfur bond. In addition, complexes **1** – **5** show geometries between that of square pyramidal and trigonal bipyramidal, whereas the protein exhibits a more purely square pyramidal geometry at the iron(II) center.

Electrochemistry

Complexes **1** – **5** were characterized by cyclic voltammetry, as shown in Figure 2. Each complex exhibits a single irreversible oxidation whose position varies with the identity of the *para* substituent on the arylthiolate ligand. We assign these anodic peaks (E_{pa}) for **1** – **5** to the $Fe^{III/II}$ couples of these complexes, and they are listed in Table 3 together with other relevant $Fe^{III/II}$ redox potentials for related complexes. Although caution must be used when analyzing irreversible waves, the trends that emerge from comparing the different values in Table 3 deserve attention. There is a clear increase in the $Fe^{III/II}$ potential for **1** – **5** as the *para* substituent changes from electron-donating to electron-withdrawing, demonstrating that the thiolate donor has a dramatic influence over the $Fe^{III/II}$ couple. It is not easy to predict a priori where fluorinated complex **4** should appear in the series, but the CV data show that $^{-}SC_6F_4$-*p*-SC_6F_5 has the weakest electron-donating ability, exhibiting an $Fe^{III/II}$ couple that is 165 mV more positive than the NO_2-substituted complex **5**. The *p*-OMe complex **3** reveals a significantly less positive oxidation potential (ΔE = 161 mV) than the related cyclam complex (Fe^{II}(Me_4[14]aneN_4)(SC_6H_4–*p*-OMe)]OTf.[60] This complex contains the same arylthiolate ligand as **3** but includes the smaller 14-membered macrocyclic N_4 donor and has N-methylated groups instead of secondary N-H groups. The change in ring size is unlikely to account for the observed difference in oxidation potentials given that the potentials for the cobalt complexes [Co[15–14]aneN_4)Cl_2]$^+$ are in the opposite order ([15]aneN_4 stabilizes Co^{II} relative to [14] aneN_4).[72] The presence of the methyl groups on the amine donors might be expected to cause the opposite shift as well. However, experimental evidence and density functional theory (DFT) calculations for [(cyclamacetate)FeF]PF_6 and (trimethylcyclamacetate)FeF]PF_6 show that the N-methylated ligand is in fact a weaker donor for both steric and electronic reasons.[73] Thus *N*-methylation may be responsible for making it significantly more difficult to oxidize (Me_4[14]aneN_4)Fe^{II}(SC_6H_4–*p*-OMe)]OTf compared to complex **3**.

The Fe^{III}/Fe^{II} redox potential for SORs isolated from different organisms have been reported to fall between 200 – 365 mV.[71,74–76] Complexes **1** – **5** and the other model complexes in Table 3 are considerably more difficult to oxidize than the enzyme. The difference between the enzyme potentials and the models in Table 3 may arise from several environmental factors, such as solvent (organic solvents for the models versus aqueous conditions for the protein), and the presence of a Glu residue in the enzyme that coordinates to the iron(III) form of the protein. There are also N-H---S bonds in the protein that would be expected to drive the redox potential towards a more positive value,[77,78] but computational models of the SOR active site show a surprising opposite effect in which the incorporation of N-H---S bonds causes a significant lowering of the $Fe^{III/II}$ redox potential.[22] Despite the discrepancies between the models and the protein, the data for **1** – **5** provide a clear trend which shows that the nature of the thiolate donor has a strong influence over the oxidation potential, as proposed for SOR.[16,22]

Reaction of Fe^{II} complexes with ROOH

In an earlier report we showed that **1** reacts at low temperature (−78 °C) with the alkylhydroperoxides tBuOOH and cumenylOOH to give the corresponding dark red, alkylperoxo-iron(III) species. Characterization of these low-temperature, metastable Fe^{III}-OOR intermediates by UV-Vis, EPR, and RR spectroscopies showed that they are low-spin (S = ½) Fe^{III}-OOR complexes with weakened Fe–O bonds. In this study we have significantly expanded this class of Fe^{III}-OOR species via the reaction of tBuOOH and cumenylOOH with complexes **2 – 5** to give low-temperature metastable Fe^{III}-OOR species.

UV-vis spectroscopy

Complexes **1 – 5** react with tBuOOH at –78 °C in CH_2Cl_2 to give the low-temperature adducts **1a – 5a** (Scheme 2). Low-temperature UV-vis spectra for these species are shown in Figure 3. The iron(II) complexes **1 – 4** are rapidly converted from colorless or light yellow to dark red upon introduction of tBuOOH at −78 °C in CH_2Cl_2. The *p*-NO_2 complex **5** is red in color because of an intraligand absorption band from the thiolate donor, and the solution of **5** changes to fuchsia upon reaction with tBuOOH at −78 °C. Each complex exhibits an intense band (ε = 1800 – 3100 $M^{-1}cm^{-1}$) between 508 and 526 nm (Figure 3), for which the peak maxima and molar absorptivity are characteristic of alkylperoxo-to-iron(III) LMCT bands.[26,29,30,79] This peak shifts to higher energy in the order **1a** (*p*-H) < **2a** (*p*-Cl) < **5a** (*p*-NO_2) < **3a** (*p*-OMe) < **4a** (SC_6F_4-*p*-SC_6F_5). This ordering follows an increase in the electron-withdrawing power of the *para* substituent and the related $Fe^{III/II}$ oxidation potential for each complex, with the exception of the *p*-OMe complex **3a**. Interestingly, the shift of the peak to higher energy for complexes **1a, 2a, 4a**, and **5a** with an increase in the $Fe^{III/II}$ couple is opposite to that observed for a series of non-thiolate ligated, polypyridyl iron(III)-hydroperoxo species.[80] The differences in the low-temperature UV-vis spectra for **1a – 5a** provide strong evidence that the thiolate ligands remain coordinated upon oxidation to the Fe^{III}-OOR species and exert a significant influence over the spectroscopic features of these species.

The UV-vis data for the *p*-NO_2 complex provides more information regarding the fate of the thiolate donor because of the intraligand band associated with $^{-}SC_6H_4$-*p*-NO_2. The UV-vis spectra of $[Fe^{II}([15]aneN_4)(SC_6H_4\text{-}p\text{-}NO_2)](BF_4)$ **5**, the corresponding Fe^{III}-OOtBu species **5a**, and the product obtained after the decay of **5a** at −78 °C are shown in Figure 4. The spectrum for the dark red iron(II) complex **5** exhibits an intense, broad band at 370 nm (blue circles). The sodium salt of the free thiolate ligand ($NaSC_6H_4$-*p*-NO_2) is also dark red in color and exhibits a peak at 422 nm in CH_2Cl_2:MeOH (99:1), which has been assigned as an intraligand transition[81,82] (data not shown). Thus coordination of $^{-}SC_6H_4$-*p*-NO_2 to Fe^{II} induces a 52 nm blue-shift of this intraligand band (blue circles), and this transition is clearly sensitive to the local environment of the sulfur atom as has been shown previously.[82] Upon reaction of **5** with tBuOOH to give the Fe^{III}-OOtBu species **5a**, the transition associated with the *p*-nitro-benzenethiolate moves to 352 nm (red triangles), concomitant with the appearance of the alkylperoxo LMCT band at 522 nm. The final spectrum exhibits a band at 327 nm that matches that of the disulfide *p*-$NO_2C_6H_4S$– SC_6H_4-*p*-NO_2 measured independently. These data indicate that the thiolate donor remains coordinated to the iron center in **5a**, giving rise to the unique band at 352 nm, which converts to disulfide upon decomposition of **5a**. Attempts to isolate the iron(III) product(s) after warming the reaction to room temperature have been unsuccessful, probably due to the decomposition of the complexes via disulfide formation.

Proposed mechanism of formation of Fe^{III}-OOR

A possible mechanism of formation of **1a – 5a, 1b, 2b, 4b** and **5b**, involves initial oxidation of the iron(II) complex by ROOH to give an Fe^{III}-OH complex, which then reacts with ROOH by displacement of OH^- to give the Fe^{III}-OOR species and H_2O. This mechanism has been proposed by Que and coworkers for the formation of similar Fe^{III}-OOR species, and in one case the identification of an Fe^{III}-OH complex $[(6\text{-}Me_3\text{-}TPA)Fe^{III}(O_2CPh)(OH)]^+$ (6-Me_3-TPA = tris(6-methyl-2-pyridylmethyl)amine) was obtained via ESI-MS after addition of 0.5 equivalents of tBuOOH to $[(6\text{-}Me_3\text{-}TPA)Fe^{II}(O_2CPh)]^+$.[83] Subsequent formation of the Fe^{III}-OOR species $[(6\text{-}Me_3\text{-}TPA)Fe^{II}(O_2CPh)]^+(OOtBu)]^+$ was observed upon addition of excess (5 equiv) tBuOOH.

According to the former mechanism, the stoichiometry of the first step should account for 0.5 equiv ROOH reacting with 1.0 equiv Fe^{II} to give the Fe^{III}-OH species, and 1.0 equiv ROOH displacing the putative OH^- ligand, resulting in a final stoichiometry of 1.5 ROOH : 1.0 Fe^{II} in the production of the alkylperoxo complex. We thus quantitated the stoichiometry of the reaction between **1** and tBuOOH to gain insight into the proposed mechanism. Successive addition of tBuOOH (0.2 equiv per addition, 4.0 M stock solution of tBuOOH in decane) to **1** at −78 °C revealed maximal formation of **1a** (λ = 526 nm) between 1.5 and 2.0 equiv of tBuOOH (Figure S1). The overall stoichiometry of tBuOOH to Fe^{II} matches well with that predicted by the former mechanism.

EPR spectroscopy

An X-band EPR spectrum collected at 15 K of the Fe^{III}-OOtBu species **2a** is shown in Figure 5, and is representative of the series **1a** – **5a**, which all show very similar EPR spectra. This spectrum is indicative of a low-spin ($S = ½$) Fe^{III} complex with axial symmetry, with g values of 2.19 and 1.97. The small signal at $g = 4.3$ is assigned to a high-spin iron(III) impurity. It was shown previously[24] that the low-spin iron(III) EPR signal for **1a** decays concomitantly with the red chromophore at −78 °C, while the high-spin iron(III) signal remains unchanged. This behavior was confirmed for **2a**, where a similar correlation for the decay of the EPR signal and red chromophore has been observed. These observations rule out the $g = 4.3$ signal as being associated with the Fe^{III}-OOR chromophore.

Analysis of Fe-O and O-O Bond Strengths from RR Spectroscopy

Definitive evidence for the identification of the low-temperature chromophores **1a** – **5a** as Fe^{III}-OOtBu species comes from RR spectroscopy (Figure 6). The dominant band in the 600 – 650 cm^{-1} range is assigned to the Fe-O stretching vibration of the Fe-OOtBu unit, while the band near 800 cm^{-1} is assigned to the O-O stretching vibration. These vibrations are resonance-enhanced with laser excitation coinciding with the alkylperoxo-to-iron(III) LMCT band. In all compounds studied here, the RR spectra obtained with a 514-nm excitation show no evidence of resonance enhanced ν(Fe–S) modes associated with the intermediate species (data not shown). The lack of enhancement of ν(Fe–S) modes suggests that the LMCT transitions have no sulfur-to-iron(III) LMCT character. The ν(O–O) falls in the expected region for a low-spin Fe^{III}-OOR (R = alkyl) species, but the ν(Fe–O) is lower than usual (Table 4). Confirmation of these assignments comes from the observed isotopic shifts for **1a**-$^{18}O^{18}$OtBu ($\nu(Fe–^{18}O)$ = 584 cm^{-1}; $\nu(^{18}O–^{18}O)$ = 757 cm^{-1}).[24] The 28- and 46-cm^{-1} downshifts observed for the $\Delta\nu(Fe–^{16/18}O)$ and $\Delta\nu(^{16/18}O–^{16/18}O)$ modes, respectively, are in perfect agreement with predicted values for isolated diatomic vibrations. Equivalent ^{18}O-shifts are observed for the ν(Fe–O) modes of **2a, 4a**, and **5a** (Figure S2). Overlapping solvent bands and a Fermi splitting of the $\nu(^{18}O–^{18}O)$ modes makes it difficult to quantify the extent of the ^{18}O-shifts on the ν(O–O), but the spectral changes observed are sufficient to confirm the assignment of the ν(O–O) mode.

Based on the RR data for **1a**, we previously noted that the Fe-O bond is surprisingly weak compared to other low-spin Fe^{III}-OOR complexes where R is an alkyl group.[24] Indeed, other low-spin Fe^{III}-OOR complexes exhibit relatively strong Fe-O bonds and weak O-O bonds,[26,29,30,79] as opposed to their high-spin analogs which give rise to weak Fe-O and strong O-O bonds.[28,31,33] The vibrational frequencies observed previously for other low-spin Fe^{III}-OOtBu complexes and those observed for **1a** – **5a** are given in Table 4. An earlier study of the low-spin complex $[Fe^{III}(TPA)(OH_n)(OOtBu)]^{n+}$ (entry 6, Table 4) showed evidence of vibrational mixing within the Fe-OOtBu unit (exptl: $\Delta^{16/18}O$ = 24 cm^{-1}; theor. diatomic approx.: $\Delta^{16/18}O$ = 31 cm^{-1}), and a normal coordinate analysis coupled with DFT calculations was used to derive a force constant of 3.53 mdyn/Å for the Fe-O bond in $[Fe^{III}(TPA)(OH_n)(OOtBu)]^{n+}$.[29] This force constant together with those of the other complexes in Table 4 are significantly larger than those for **1a** – **5a**. The **1a** to **5a** series presents weaker Fe-O bonds than other iron(III)-alkylperoxo complexes lacking the thiolate ligand and implicates the unique thiolate donor in weakening this bond.

The influence of the sulfur donor can be seen in the correlation between the energy of the Fe-O vibrations for **1a** – **5a** and the identity of the thiolate ligand. Specifically, the ν(Fe-O) shifts to higher energy as the electron-withdrawing character of the aryl group increases. In contrast, the ν(O-O) is unaffected by the thiolate donor, and the $k_{\text{O-O}}$ is nearly constant in the **1a** – **5a** series and is similar to those of previously reported low-spin complexes lacking a thiolate ligand (Table 4). These RR data show that the electron-donating ability of the arylthiolate ligand controls the strength of the Fe-O bond without affecting the O-O bond.

A similar dependence on the electron-donating ability of the arylthiolate ligand is observed for the Fe^{III}-OOCm (Cm = $C(CH_3)_2C_6H_5$) species. The RR spectra of these complexes show ν (Fe-O) modes between 622 and 631 cm^{-1} (Figure 7) which are ~10 cm^{-1} higher than in the Fe-OOtBu complexes. As with the Fe-OOtBu complexes, the $\text{Fe}^{\text{III}}\text{–}^{18}\text{O}^{18}\text{OCm}$ complexes show RR spectra that confirm the ν(Fe-O) assignment, but the extent of the isotope shifts come short of the expected values for isolated diatomic vibrations and suggest that mode mixing occurs with the cumenyl derivatives (Figure S3). The frequency up-shifts observed with the ν (Fe-O) may be due to the different steric requirements of the cumenyl group versus the *tert*-butyl group and conformational changes in the Fe-OOR moiety. Despite these changes, and as seen earlier with the tBu series, the Fe-O stretching frequencies increase with increasing electron-withdrawing character from the para-substituent on the arylthiolate ligand. Once again, these results support a *trans* effect of the thiolate donor, where both σ- and π-bonding interactions between the iron(III) ion and the alkylperoxo ligand are weakened by the thiolate donor competing for the same metal *d* orbitals.

Theoretical calculations on the alkylperoxo species were carried out to obtain further insights into the trends observed in the vibrational data. Density functional theory calculations (B3LYP/6-311G)[56] were performed on a model of the alkylperoxo intermediates in which the tBu or Cm group was replaced with a methyl group, $[(\text{Fe}^{\text{III}}([15]\text{aneN}_4)(\text{OOMe})(\text{SAr})]^+$. The geometries were optimized beginning from the X-ray structural coordinates of the corresponding iron(II) starting materials, and both high-spin and low-spin iron(III) configurations (S = 5/2 or 1/2) were evaluated. The low-spin species were found to be the lowest in energy for all five thiolate ligands.[84] The calculated vibrational frequencies for the low-spin complexes reveal that the Fe-O stretch strengthens upon decreasing the electron-donating ability of the thiolate donor, whereas the O-O stretch shows less variation: SAr (ν (Fe-O), ν(O-O)) = SC_6H_4-*p*-OMe (586, 776 cm^{-1}); SC_6H_5 (584, 774 cm^{-1}); SC_6H_4-*p*-Cl (595, 781 cm^{-1}); SC_6H_4-*p*-NO_2 (599, 775 cm^{-1}); SC_6F_4-*p*-SC_6F_5 (600, 776 cm^{-1}). The calculated Fe-O distances also vary with the arylthiolate substituents, becoming shorter with decreasing electron-donating character, while the O-O distance shows no such correlation: SAr (*d*(Fe-O), *d*(O-O)) = SC_6H_4-*p*-OMe (1.875, 1.532 Å); SC_6H_5 (1.873, 1.532 Å); SC_6H_4-*p*-Cl (1.870, 1.532 Å); SC_6H_4-*p*-NO_2 (1.864, 1.531 Å); SC_6F_4-*p*-SC_6F_5 (1.858, 1.530 Å). These findings are in agreement with the trends observed experimentally for the Fe-O and O-O vibrations with changes in the identity of the thiolate ligand, and support the idea that the thiolate donor modulates the strength of the Fe-O bond in the alkylperoxo species.

The $[15]\text{aneN}_4$ ligand, as well as related macrocycles such as $[14]\text{aneN}_4$ (cyclam), are flexible and potentially allow for both *cis* and *trans* geometries in complexes of the type [M (macrocycle)L_2], depending on the size of the metal ion and nature of the coligands L. Although there are no structurally well-defined iron(III) complexes of the $[15]\text{aneN}_4$ ligand,[85] there are a number of other six-coordinate M^{III} complexes ($[M^{\text{III}}([15]\text{aneN}_4)L_2]$ (M = Co, Cr, Rh; L = monodentate ligand)). [46,72,86–88] All of these complexes exist exclusively in the *trans* geometry, as opposed to smaller macrocycles such as cyclam, which exhibit both *cis*- and *trans*-isomers for complexes of the type $[M^{III}(cyclam)L_2]$. Molecular mechanics calculations from Busch and Hay indicated that the *trans* geometry is energetically preferred for the [15] aneN_4 ligand, providing a proper "fit" around the metal center.[72,86] Thus we conclude that the thiolate ligands in the **Fe-OOR** complexes are coordinated *trans* to the **OOR** ligand and are weakening the Fe-O interaction through a *trans* effect.

Our spectroscopic study of these Fe-OOR complexes shows that low-spin iron(III) centers do not necessarily give rise to strong Fe-O bonds in Fe^{III}-OOR species. Interestingly, a weakened Fe-O bond was also recently observed by Kovacs and coworkers for the *high-spin* complex $[Fe^{III}(cyclam\text{-}PrS)(OOH)]^+$, and was attributed to a *trans* influence of the thiolate donor.[36] These observations contrast with a series of high-spin Fe^{III}-OOR complexes $[(L^8py\text{-}_2)(X)Fe^{III}(OOR)]^+$ (L^8py_2 = neutral N_4 donor, X = CH_3-*p*-$C_6H_4S^-$, $C_6H_5CO_2^-$, OTf^-), where the N_4 ligand enforces a trans X-Fe-OOR arrangement, and where the Fe-O bond is not affected by the nature of the trans ligand.[33] The $[Fe^{III}(cyclam\text{-}PrS)(OOH)]^+$ complex is currently unique among *high-spin* Fe^{III}-OOH species in exhibiting the same *trans* influence on the Fe-O bond as observed in **1a** – **5a, 1b, 2b, 4b**, and **5b**. It should be noted that with the exception of $[Fe^{III}(cyclam\text{-}PrS)(OOH)]^+$, all *trans*-$[Fe^{III}(cyclam)L_2]$ complexes are found in low-spin configurations. For example, even the very weak-field donor OTf^- yields low-spin iron(III) in [*trans*-(cyclam-acetato)$Fe^{III}(OTf)]^+$,[89] whereas *cis*-$[Fe^{III}(cyclam)L_2]$ complexes are uniformly high-spin. Although a *cis* configuration for $[Fe^{III}(cyclam\text{-}PrS)(OOH)]^+$ can not be entirely ruled out based on the available data, as described this complex provides another example of a thiolate-induced *trans* influence for an Fe-OO(H or R) species.

Implications for the SOR mechanism

Examination of the reaction between native SOR and O_2^- generated by pulse radiolysis by different research groups has led to the observation of a transient intermediate characterized by a UV-vis band with λ_{max} = 600 nm.[14,17,19,21,90] Kurtz has recently reported the generation of this same 600 nm intermediate by stopped-flow mixing of SOR and KO_2.[91] This intermediate has been proposed to be an Fe^{III}-OO(H) species, but has thus far eluded characterization by other spectroscopic methods. However, reaction of SOR with H_2O_2 has allowed for the trapping and characterization of an Fe^{III}-peroxo species, initially formulated as an $Fe^{III}\text{-}\eta^2\text{-}O_2^{2-}$ ("side-on" peroxo) species.[92,93] High-resolution X-ray structural data has become available on a mutant SOR (E114A) in which the crystals were first oxidized to Fe^{III} and then soaked in H_2O_2 prior to freezing.[15] The structural data revealed a terminal, "end-on" bound hydroperoxo-iron(III) species trapped in different configurations. Earlier predictions from density functional theory (DFT) calculations suggested that a side-on peroxide bonding mode was not sterically feasible for the SOR active site and favored a low-spin, end-on Fe^{III}-OOH species.[94] These calculations combined with the recent X-ray structural analysis argue for assignment of the species generated in solution between SOR and H_2O_2 as a terminally-bound Fe^{III}-OOH species. New DFT calculations from Solomon and coworkers,[22] which take into account the influence of the putative N-H---S^{Cys} hydrogen bonds in SOR, also predicts an end-on, protonated peroxide (Fe^{III}-OOH) as the first detectable intermediate in the catalytic mechanism, although these calculations favor a high-spin Fe^{III} ground state as opposed to the low-spin Fe^{III}-OOH predicted in the earlier DFT study.[94]

Although the relationship of the H_2O_2-derived species to the native catalytic pathway is an open question, analysis of the structural and spectroscopic data of the H_2O_2-derived intermediate has provided valuable information regarding the inherent properties of an Fe-(hydro)peroxo moiety in the SOR active site. Most pertinent to the present study is recent work by Nivière and coworkers, who sought to determine the role of the cysteine donor by examining a H_2O_2-derived intermediate for a mutant form of SOR from *D. baarsii* in which the iron-sulfur bond was perturbed.[18] In this study Glu[114], which is found in proximity to the Fe-S bond, was replaced with Ala, causing a disruption of the dipolar interaction between Glu[114] and the Fe-S unit. In the oxidized form of the mutant (obtained by treating the mutant with K_2IrCl_6), a downshift of the Fe^{3+}-S vibrational modes (291/313/311 cm^{-1} for E114A; 299/316/323 for wild-type) was observed, indicating a significant weakening of the iron-sulfur bond. Reaction of the reduced form of the mutant with a slight excess of H_2O_2 followed by rapid freezing (< 5 s) allowed for freeze-trapping of an iron-peroxo intermediate and subsequent examination by RR spectroscopy. The RR spectrum showed intense ν(Fe-O) and ν(O-O) bands at 446 cm^{-1} and 851 cm^{-1}. In comparison, RR data on H_2O_2-derived intermediates from both wild-type and E47A–SOR revealed lower Fe-O stretching frequencies (ν(Fe-O) = 438 cm^{-1}) but the same O-O stretch (ν(O-O) = 850–851 cm^{-1}). Thus a major conclusion from this work was that the E114A mutation induces a weakening of the Fe-S bond, *which in turn causes* a *significant strengthening of the Fe-O bond in the (hydro)peroxo intermediate, but no change in the O-O bond*.

The results presented herein are strikingly similar to the recent findings for the E114A mutant of the enzyme; namely that the weakening of the arylthiolate donor in $[Fe^{III}([15]aneN_4)(SAr)(OOR)]^+$ induces a significant strengthening of the Fe-O bond, while leaving the O-O bond unperturbed. Although these Fe^{III}-OOR model complexes are low-spin, while the Fe^{III}-OOH intermediate in E114A SOR is suggested to be high-spin, our results provide strong evidence to support the hypothesis that the *trans* thiolate donor in SOR significantly modulates the strength of the Fe-O bond.

In addition to modulation of the Fe-O bond strength for E114A SOR, the stability of the Fe-OO(H) intermediate was also significantly increased with the weakening of the Fe-S interaction, as demonstrated by increased yields of the intermediate and slower decay kinetics.[18] The kinetics of decay for **2a – 5a** are complicated and do not follow a simple first-order rate law. Similarly, complex kinetic profiles were previously observed for the decay of other low-spin Fe^{III}-OOtBu complexes.[26] However, monitoring the disappearance of the LMCT bands for **1a – 5a** by low-temperature UV-vis reveal a qualitative trend wherein the Fe^{III}-OOR species decay more slowly as the electron-donating character of ArS^- is reduced. For example, the fluorinated derivative **4a** exhibits a remarkably slow decay rate, showing almost no decomposition at −78 °C for over 48 h, as opposed to 1.5 h for the complete decay of the *p*-H complex **1a**. As described in the Introduction (vide supra), a study by Que and Halfen on the high-spin model complexes $(N_4L)Fe^{III}$-OOR ($L = {}^-OTf$, ${}^-O_2CC_6H_5$, ${}^-SC_6H_4$-p-CH_3)[33] showed an *increased* stability with *electron-donating trans* axial ligands (for $k_{decomposition}$, $L = {}^-OTf > {}^-O_2CC_6H_5 > {}^-SC_6H_4$-$p$-$CH_3$) and no impact of the trans ligand on the ν(Fe-O) in the RR spectra. Indeed, to our knowledge compounds **1a – 5a** are the first series of model complexes that provide direct evidence for such a *trans* influence in Fe^{III}-OO(H or R) species.

Summary and Perspective

We have prepared a series of iron(II) complexes as models of the SOR active site. These complexes were designed to examine the influence of the thiolate donor on the structural and physical properties as well as the reactivity of the metal center at parity of ligand environment. The metrical parameters as determined by X-ray crystallography do not vary significantly with the change in thiolate donor. In contrast, the nature of the arylthiolate donor has a significant impact on the Fe^{III}/Fe^{II} potential, in support of the suggestion that the cysteine ligand in SOR plays a major role in controlling the iron redox potential.[16,22] The stabilization of Fe^{III}-OOR species at low temperature for all of the thiolate-ligated complexes was demonstrated, and spectroscopic characterization of these alkylperoxo complexes shows that they are low-spin iron(III) species with weak Fe-O bonds. These findings provide an exception to the hypothesis that low-spin Fe^{III}-OO(H or R) species necessarily exhibit strong Fe-O bonds in comparison to their high-spin counterparts.

The electron-donating power of the sulfur donor in the Fe^{III}-OOR complexes described herein directly influences the strength of the Fe-O bond through a *trans* influence from the thiolate ligand. In contrast, the thiolate donor does not impact the O-O bond strength. DFT calculations on a simplified model for the Fe^{III}-OOR complexes support these experimental findings. A similar observation was recently described for the E114A SOR enzyme, in which a H_2O_2-derived Fe^{III}-OO(H) species was trapped and characterized by RR spectroscopy.[18] Thus, our results, combined with the results for E114A SOR suggest that an important function of the Cys donor in SOR is to weaken the Fe-O bond without weakening the O-O bond, thereby favoring Fe-O over O-O bond cleavage. Recent DFT calculations on SOR also support this conclusion.[22]

The sulfur atom of the Cys ligand in SOR is within weak hydrogen bond contact of two nearby amide N-H groups as determined by X-ray crystallography.[20] For many other cysteine-ligated iron proteins it has been proposed that N-H---S hydrogen bonds assist in tuning the S-Fe bonding interaction and the iron redox potentials,[78] and similar proposals have been made for SOR.[20,22] We suggest that perhaps the presence of the N-H---S bonds in SOR help to modulate the Fe-S interaction in much the same way as addition of an electron-withdrawing *para* substituent to the arylthiolate ligand of our model system; they provide fine-tuning of the Cys ligand's ability to influence the Fe-O bond while leaving the O-O bond unperturbed in an Fe^{III}-OOH intermediate, ultimately favoring protonation and formation of H_2O_2. Generation of Fe^{III}-OO(H) adducts via reactions between our model complexes and H_2O_2 and O_2^- is currently being examined.

Supplementary Material

Refer to Web version on PubMed Central for supplementary material.

Acknowledgements

D.P.G. is grateful to the National Institute of General Medical Sciences at the NIH for funding this work (GM62309). F. N. is thankful for financial support provided by a Zeltmann Fellowship sponsored through Johns Hopkins University. Prof. V. Szalai (University of Maryland Baltimore County) is acknowledged for her help with EPR spectroscopy. We thank Dr. Andrea Caneschi (University of Florence) for collecting SQUID data.

References

1. Sono M, Roach MP, Coulter ED, Dawson JH. Chem. Rev 1996;96:2841–2887. [PubMed: 11848843]
2. Sligar SG, Makris TM, Denisov IG. Biochem. Biophys. Res. Comuun 2005;338:346–354.
3. Shaik S, Kumar D, de Visser SP, Altun A, Thiel W. Chem. Rev 2005;105:2279–2328. [PubMed: 15941215]
4. Meunier B, de Visser SP, Shaik S. Chem. Rev 2004;104:3947–3980. [PubMed: 15352783]
5. Loew GH, Harris DL. Chem. Rev 2000;100:407–419. [PubMed: 11749241]
6. Denisov IG, Makris TM, Sligar SG, Schlichting I. Chem. Rev 2005;105:2253–2277. [PubMed: 15941214]
7. Unno M, Matsui T, Ikeda-Saito M. Nat. Prod. Rep 2007;24:553–570. [PubMed: 17534530]
8. Stubbe J, Kozarich JW, Wu W, Vanderwall DE. Acc. Chem. Res 1996;29:322–330.
9. Stubbe J, Kozarich JW. Chem. Rev 1987;87:1107–1136.
10. Que L Jr, Ho RYN. Chem. Rev 1996;96:2607–2624. [PubMed: 11848838]
11. Kovaleva EG, Neibergall MB, Chakrabarty S, Lipscomb JD. Acc. Chem. Res 2007;40:475–483. [PubMed: 17567087]

12. Kovaleva EG, Lipscomb JD. Science 2007;316:453–457. [PubMed: 17446402]
13. Costas M, Mehn MP, Jensen MP, Que L Jr. Chem. Rev 2004;104:939–986. [PubMed: 14871146]
14. Emerson JP, Coulter ED, Cabelli DE, Phillips RS, Kurtz DM Jr. Biochemistry 2002;41:4348–4357. [PubMed: 11914081]
15. Katona G, Carpentier P, Nivière V, Amara P, Adam V, Ohana J, Tsanov N, Bourgeois D. Science 2007;316:449–453. [PubMed: 17446401]
16. Kurtz DM Jr. Acc. Chem. Res 2004;37:902–908. [PubMed: 15612680]
17. Lombard M, Houée-Levin C, Touati D, Fontecave M, Nivière V. Biochemistry 2001;40:5032–5040. [PubMed: 11305919]
18. Mathé C, Weill CO, Mattioli TA, Berthomieu C, Houée-Levin C, Tremey E, Nivière V. J. Biol. Chem 2007;282:22207–22216. [PubMed: 17545670]
19. Nivière V, Lombard M, Fontecave M, Houée-Levin C. Febs Letters 2001;497:171–173. [PubMed: 11377434]
20. Adam V, Royant A, Nivière V, Molina-Heredia FP, Bourgeois D. Structure 2004;12:1729–1740. [PubMed: 15341736]
21. Coulter ED, Emerson JP, Kurtz DM Jr, Cabelli DE. J. Am. Chem. Soc 2000;122:11555–11556.
22. Dey A, Jenney FE, Adams MWW, Johnson MK, Hodgson KO, Hedman B, Solomon EI. J. Am. Chem. Soc 2007;129:12418–12431. [PubMed: 17887751]
23. Kovacs JA, Brines LM. Acc. Chem. Res 2007;40:501–509. [PubMed: 17536780]
24. Krishnamurthy D, Kasper GD, Namuswe F, Kerber WD, Sarjeant AAN, Moenne-Loccoz P, Goldberg DP. J. Am. Chem. Soc 2006;128:14222–14223. [PubMed: 17076472]
25. Girerd JJ, Banse F, Simaan AJ. Struct. Bonding (Berlin) 2000;97:145–177.
26. Jensen MP, Payeras AMI, Fiedler AT, Costas M, Kaizer J, Stubna A, Munck E, Que L Jr. Inorg. Chem 2007;46:2398–2408. [PubMed: 17326618]
27. Lehnert N, Fujisawa K, Solomon EI. Inorg. Chem 2003;42:469–481. [PubMed: 12693229]
28. Lehnert N, Ho RYN, Que L Jr, Solomon EI. J. Am. Chem. Soc 2001;123:12802–12816. [PubMed: 11749538]
29. Lehnert N, Ho RYN, Que L Jr, Solomon EI. J. Am. Chem. Soc 2001;123:8271–8290. [PubMed: 11516278]
30. Menage S, Wilkinson EC, Que L Jr, Fontecave M. Angew. Chem. Int. Ed 1995;34:203–205.
31. Wada A, Ogo S, Watanabe Y, Mukai M, Kitagawa T, Jitsukawa K, Masuda H, Einaga H. Inorg. Chem 1999;38:3592–3593. [PubMed: 11671111]
32. Zang Y, Kim J, Dong YH, Wilkinson EC, Appelman EH, Que L Jr. J. Am. Chem. Soc 1997;119:4197–4205.
33. Bukowski MR, Halfen HL, van den Berg TA, Halfen JA, Que L Jr. Angew. Chem. Int. Ed 2005;44:584–587.
34. Clay MD, Cosper CA, Jenney FE, Adams MWW, Johnson MK. Proc. Natl. Acad. Sci. U.S.A 2003;100:3796–3801. [PubMed: 12655067]
35. Kovacs JA. Chem. Rev 2004;104:825–848. [PubMed: 14871143]
36. Kitagawa T, Dey A, Lugo-Mas P, Benedict JB, Kaminsky W, Solomon E, Kovacs JA. J. Am. Chem. Soc 2006;128:14448–14449. [PubMed: 17090014]
37. Kokatnur VR, Jelling M. J. Am. Chem. Soc 1941;63:1432–1433.
38. Walling C, Buckler SA. J. Am. Chem. Soc 1955;77:6032–6038.
39. Finn MG, Sharpless KB. J. Am. Chem. Soc 1991;113:113–126.
40. CRysalis, CrysAlis PRO. Poland: Oxford Diffraction Ltd. Wroclaw;
41. Sheldrick, GM. SHELXTL, Version 6.10. Madison, Wisconsin, USA: Bruker AXS Inc.; 2000.
42. Ballester L, Gutierrez A, Perpinan MF, Sanchez AE, Azcondo MT, Gonzalez MJ. Inorg. Chim. Acta 2004;357:1054–1062.
43. Blake AJ, Li WS, Lippolis V, Schroder M. Acta. Cryst 1998;C54:299–302.
44. Chen LF, Cotton FA. J. Mol. Struct 1998;470:161–166.
45. Clegg W. Acta. Cryst 1986;C42:1463–1464.

46. Clegg W, Leupin P, Richens DT, Sykes AG, Raper ES. Acta. Cryst 1985;C41:530–532.
47. Ito T, Kato M, Ito H. Bull. Chem. Soc. Jpn 1984;57:2634–2640.
48. Ito T, Kato M, Ito H. Bull. Chem. Soc. Jpn 1984;57:2641–2649.
49. Jacobsen CJH, Hyldtoft J, Larsen S, Pedersen E. Inorg. Chem 1994;33:840–842.
50. Kato M, Ito T. Inorg. Chem 1985;24:509–514.
51. Mak TCW, Che CM, Wong KY. J. Chem. Soc., Chem. Commun 1985:986–988.
52. Notni J, Gorls H, Anders E. Eur. J. Inorg. Chem 2006:1444–1455.
53. Panneerselvam K, Lu TH, Chi TY, Pariya C, Liao FL, Chung CS. Acta. Cryst 1998;C54:712–714.
54. Pleus RJ, Saak W, Pohl SZ. Anorg. Allg. Chem 2001;627:250–253.
55. Shi S, Espenson JH, Bakac A. J. Am. Chem. Soc 1990;112:1841–1846.
56. Frisch MJ, et al. Gaussian 03, Revision C.02. 2004
57. Green MT. J. Am. Chem. Soc 2006;128:1902–1906. [PubMed: 16464091]
58. Namuswe F, Sarjeant AAN, Goldberg DP. unpublished results.
59. Halfen JA, Moore HL, Fox DC. Inorg. Chem 2002;41:3935–3943. [PubMed: 12132918]
60. Fiedler AT, Halfen HL, Halfen JA, Brunold TC. J. Am. Chem. Soc 2005;127:1675–1689. [PubMed: 15701002]
61. Shearer J, Scarrow RC, Kovacs JA. J. Am. Chem. Soc 2002;124:11709–11717. [PubMed: 12296737]
62. Shearer J, Nehring J, Lovell S, Kaminsky W, Kovacs JA. Inorg. Chem 2001;40:5483–5484. [PubMed: 11599942]
63. The high-spin configuration for 1 – 3 has been confirmed by SQUID measurements, giving $\chi_M T$ = 3.61 – 3.70 cm^3 mol^{-1} K at 298 K (χ_MT(theor.) = 3.63 cm^3 mol^{-1} K with g = 2.2 for HS Fe^{II})]
64. Krishnamurthy D, Sarjeant A, Goldberg DP, Caneschi A, Totti F, Zakharov LN, Rheingold AL. Chem. Eur. J 2005;11:7328–7341.
65. Mukherjee RN, Abrahamson AJ, Patterson GS, Stack TDP, Holm RH. Inorg. Chem 1988;27:2137–2144.
66. Zang Y, Que L Jr. Inorg. Chem 1995;34:1030–1035.
67. Addison AW, Rao TN, Reedjik J, van Rijn J, Verschoor GC. J. Chem. Soc., Dalton Trans 1984:1349–1456.
68. McNaughton RL, Tipton AA, Rubie ND, Conry RR, Kirk ML. Inorg. Chem 2000;39:5697–5706. [PubMed: 11151370]
69. Solomon EI, Szilagyi RK, George SD, Basumallick L. Chem. Rev 2004;104:419–458. [PubMed: 14871131]
70. Yeh AP, Hu YL, Jenney FE Jr, Adams MWW, Rees DC. Biochemistry 2000;39:2499–2508. [PubMed: 10704199]
71. Clay MD, Jenney FE Jr, Hagedoorn PL, George GN, Adams MWW, Johnson MK. J. Am. Chem. Soc 2002;124:788–805. [PubMed: 11817955]
72. Hung Y, Martin LY, Jackels SC, Tait AM, Busch DH. J. Am. Chem. Soc 1977;99:4029–4039.
73. Berry JF, Bill E, Garcia-Serres R, Neese F, Weyhermuller T, Wieghardt K. Inorg. Chem 2006;45:2027–2037. [PubMed: 16499363]
74. Jovanovic T, Ascenso C, Hazlett KRO, Sikkink R, Krebs C, Litwiller R, Benson LM, Moura I, Moura JJG, Radolf JD, Huynh BH, Naylor S, Rusnak F. J. Biol. Chem 2000;275:28439–28448. [PubMed: 10874033]
75. Rodrigues JV, Saraiva LM, Abreu IA, Teixeira M, Cabelli DE. J. Biol. Inorg. Chem 2007;12:248–256. [PubMed: 17066300]
76. Tavares P, Ravi N, Moura JJG, Legall J, Huang YH, Crouse BR, Johnson MK, Huynh BH, Moura I. J. Biol. Chem 1994;269:10504–10510. [PubMed: 8144635]
77. Okamura T, Takamizawa S, Ueyama N, Nakamura A. Inorg. Chem 1998;37:18–28. [PubMed: 11670255]
78. Dey A, Okamura T, Ueyama N, Hedman B, Hodgson KO, Solomon EI. J. Am. Chem. Soc 2005;127:12046–12053. [PubMed: 16117545]

79. Jensen MP, Costas M, Ho RYN, Kaizer J, Payeras AMI, Munck E, Que L Jr, Rohde JU, Stubna A. J. Am. Chem. Soc 2005;127:10512–10525. [PubMed: 16045338]
80. Roelfes G, Vrajmasu V, Chen K, Ho RYN, Rohde JU, Zondervan C, la Crois RM, Schudde EP, Lutz M, Spek AL, Hage R, Feringa BL, Münck E, Que L Jr. Inorg. Chem 2003;42:2639–2653. [PubMed: 12691572]
81. Abu-Eittah RH, Hilal RH. Appl. Spectrosc 1972;26:270–277.
82. Thompson JS, Marks TJ, Ibers JA. J. Am. Chem. Soc 1979;101:4180–4192.
83. Kim J, Zang Y, Costas M, Harrison RG, Wilkinson EC, Que L Jr. J. Biol. Inorg. Chem 2001;6:275–284. [PubMed: 11315563]
84. It should be noted that there are difficulties in determining the relative energies of spin states for open-shell metal ions by DFT calculations
85. Hay RW, Fraser I. Polyhedron 1997;16:2223–2227.
86. Hay RW, Tarafder MTH. J. Chem. Soc., Dalton Trans 1991:823–827.
87. Islam MS, Uddin MM. Polyhedron 1993;12:423–426.
88. Bhattacharya PK. J. Chem. Soc., Dalton Trans 1980:810–812.
89. Grapperhaus CA, Mienert B, Bill E, Weyhermuller T, Wieghardt K. Inorg. Chem 2000;39:5306–5317. [PubMed: 11187471]
90. Rodrigues JV, Abreu IA, Cabelli D, Teixeira M. Biochemistry 2006;45:9266–9278. [PubMed: 16866373]
91. Huang VW, Emerson JP, Kurtz DM. Biochemistry 2007;46:11342–11351. [PubMed: 17854204]
92. Mathé C, Mattioli TA, Horner O, Lombard M, Latour JM, Fontecave M, Nivière VJ. Am. Chem. Soc 2002;124:4966–4967.
93. Horner O, Mouesca JM, Oddou JL, Jeandey C, Nivière V, Mattioli TA, Mathé C, Fontecave M, Maldivi P, Bonville P, Halfen JA, Latour JM. Biochemistry 2004;43:8815–8825. [PubMed: 15236590]
94. Silaghi-Dumitrescu R, Silaghi-Dumitrescu L, Coulter ED, Kurtz DM Jr. Inorg. Chem 2003;42:446–456. [PubMed: 12693226]

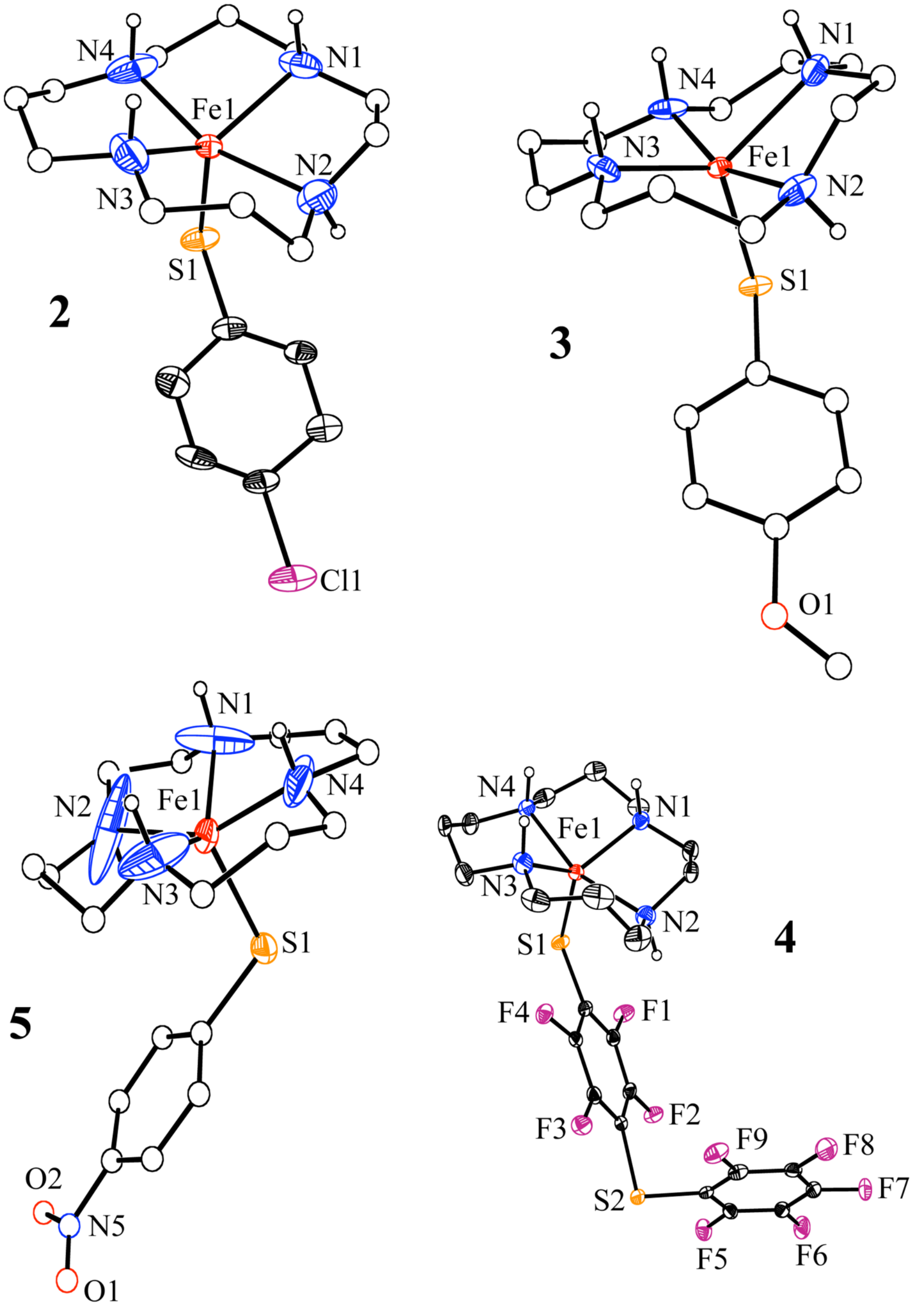

Figure 1.

ORTEP diagrams of the complex cations of **2, 3, 4** and **5** showing 30% probability ellipsoids. Hydrogen atoms were omitted for clarity except for the N-H groups. The carbon atoms for the macrocycle in **2, 3**, and **5** as well as the phenyl substituents of **3** and **5** are drawn as isotropic spheres for clarity.

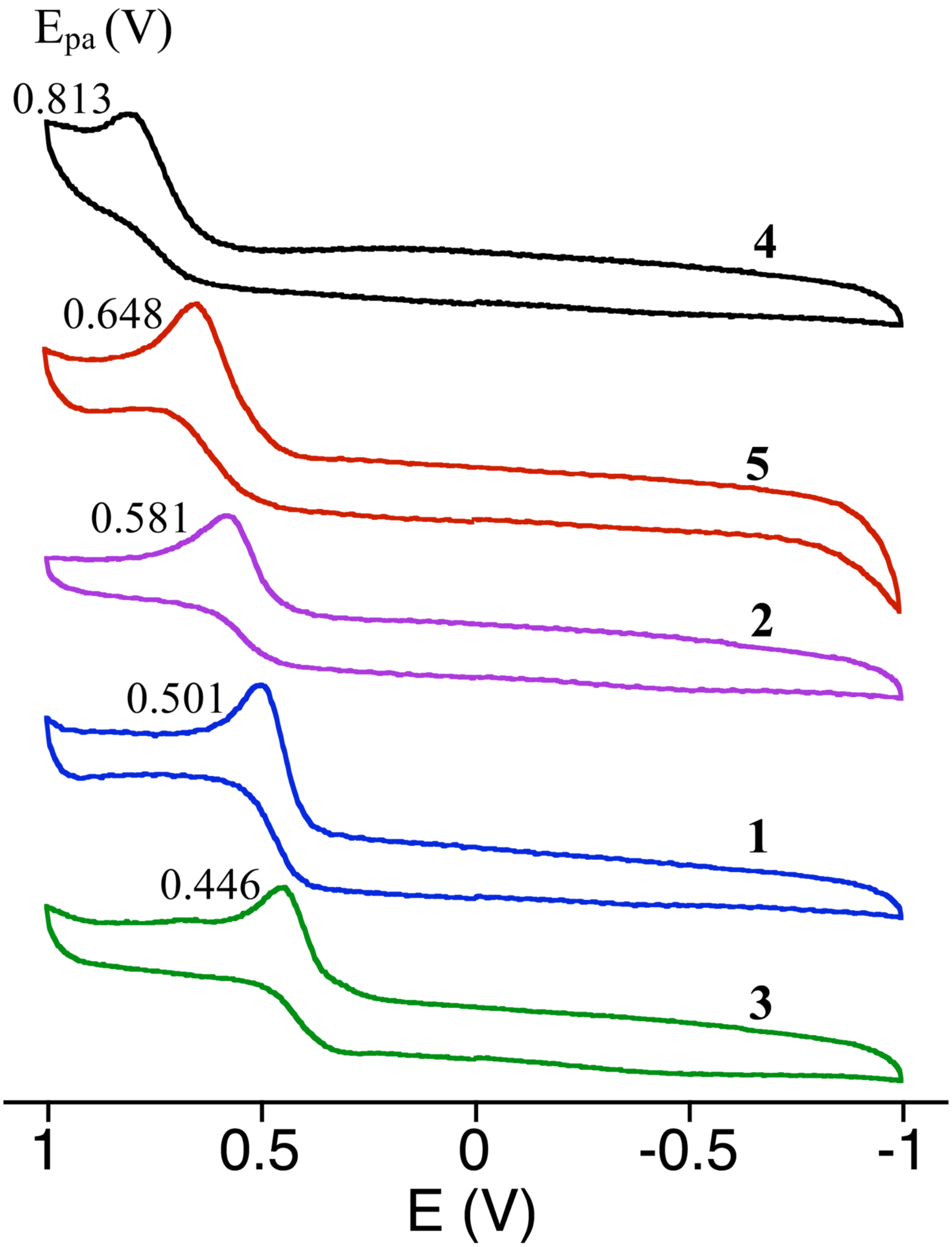

Figure 2.

Cyclic voltammograms for [Fe^{II}([15]aneN$_4$)(SC$_6$H$_4$*p*-X)]BF$_4$ (X = H (**1**), Cl (**2**), OMe (**3**), NO$_2$ (**5**)) and [Fe^{II}([15]aneN$_4$)(SC$_6$F$_4$*p*-SC$_6$F$_5$)]BF$_4$ (**4**), measured in CH$_2$Cl$_2$ using a Ag/AgCl reference electrode (3.5 M KCl).

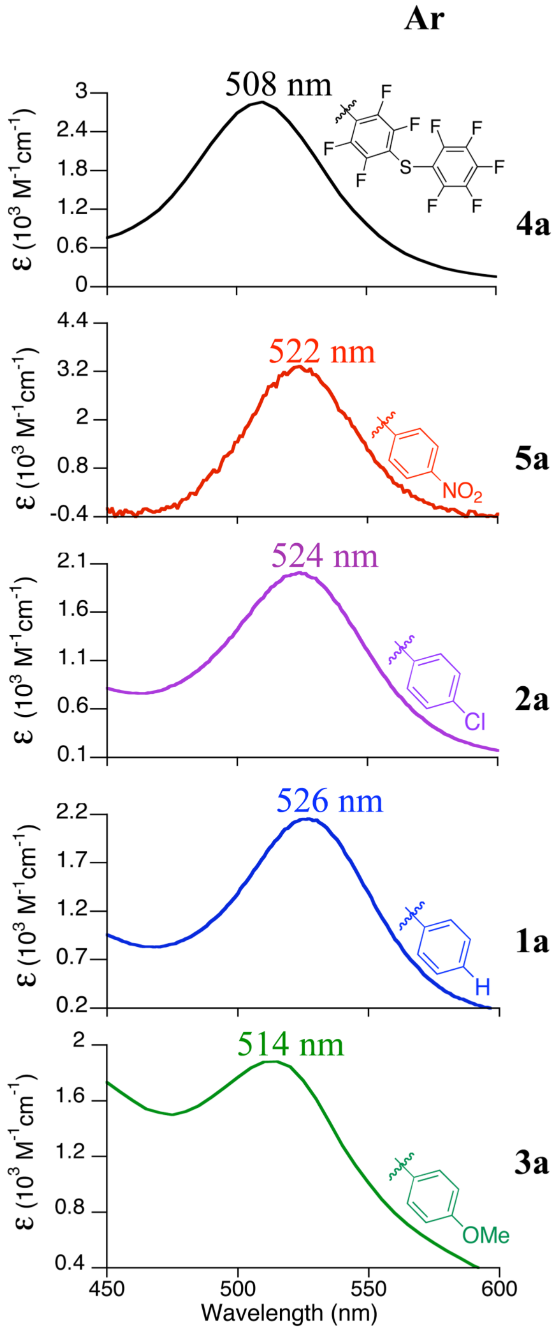

Figure 3.

UV-vis spectra of [Fe^{III}([15]aneN$_4$)(SAr)(OO^{t}Bu)]$^+$ complexes **1a – 5a** in CH$_2$Cl$_2$ at −78 °C.

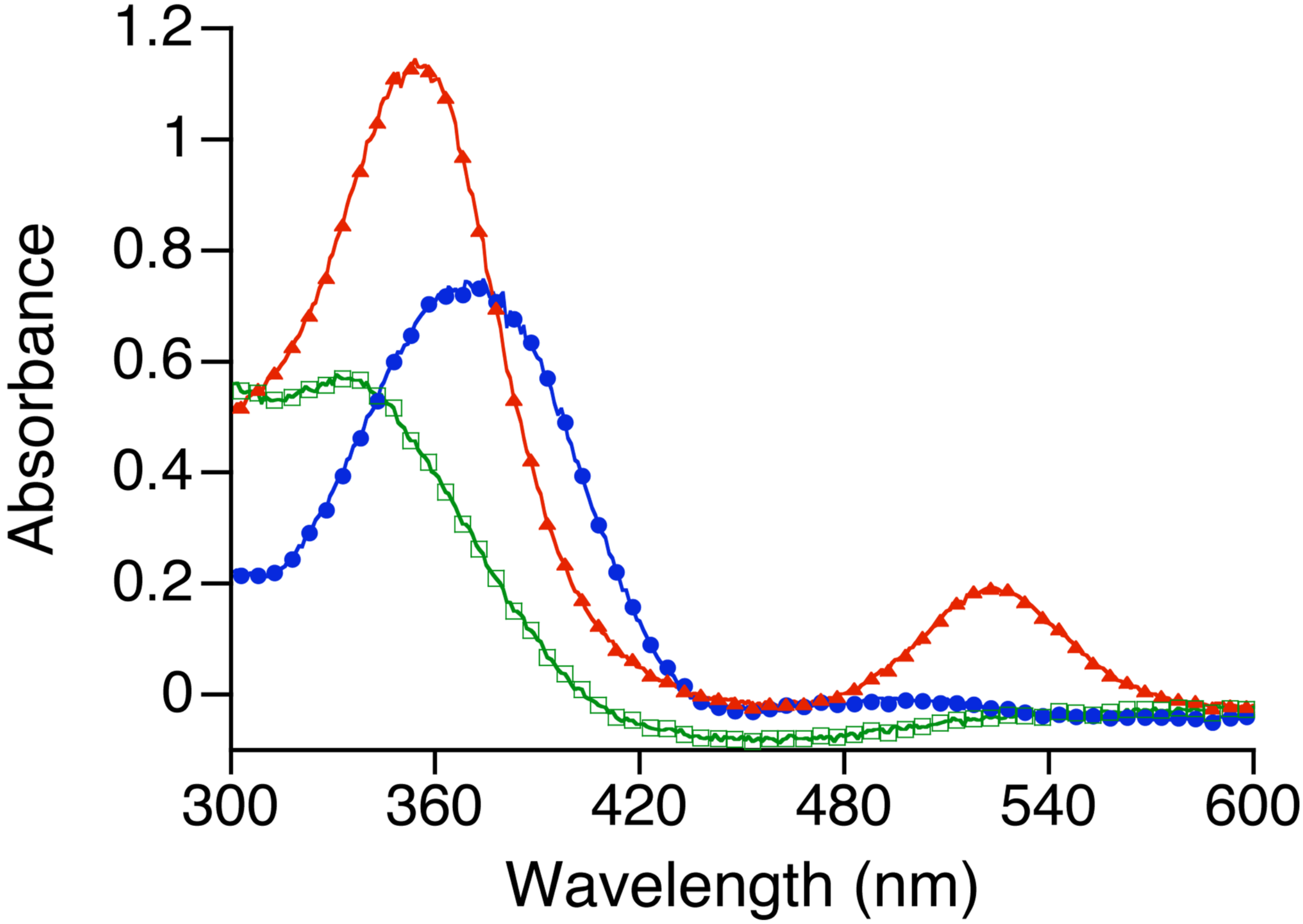

Figure 4.

UV-vis spectra of [Fe^{II}([15]aneN$_4$)(SC$_6$H$_4$*p*-NO$_2$)]BF$_4$**(5)** (**blue circles**), [Fe^{III}([15]aneN$_4$)(SC$_6$H$_4$*p*-NO$_2$)(OO^{t}Bu)]$^+$ (**5a**) (**red triangles**) and the decomposition product (**green squares**).

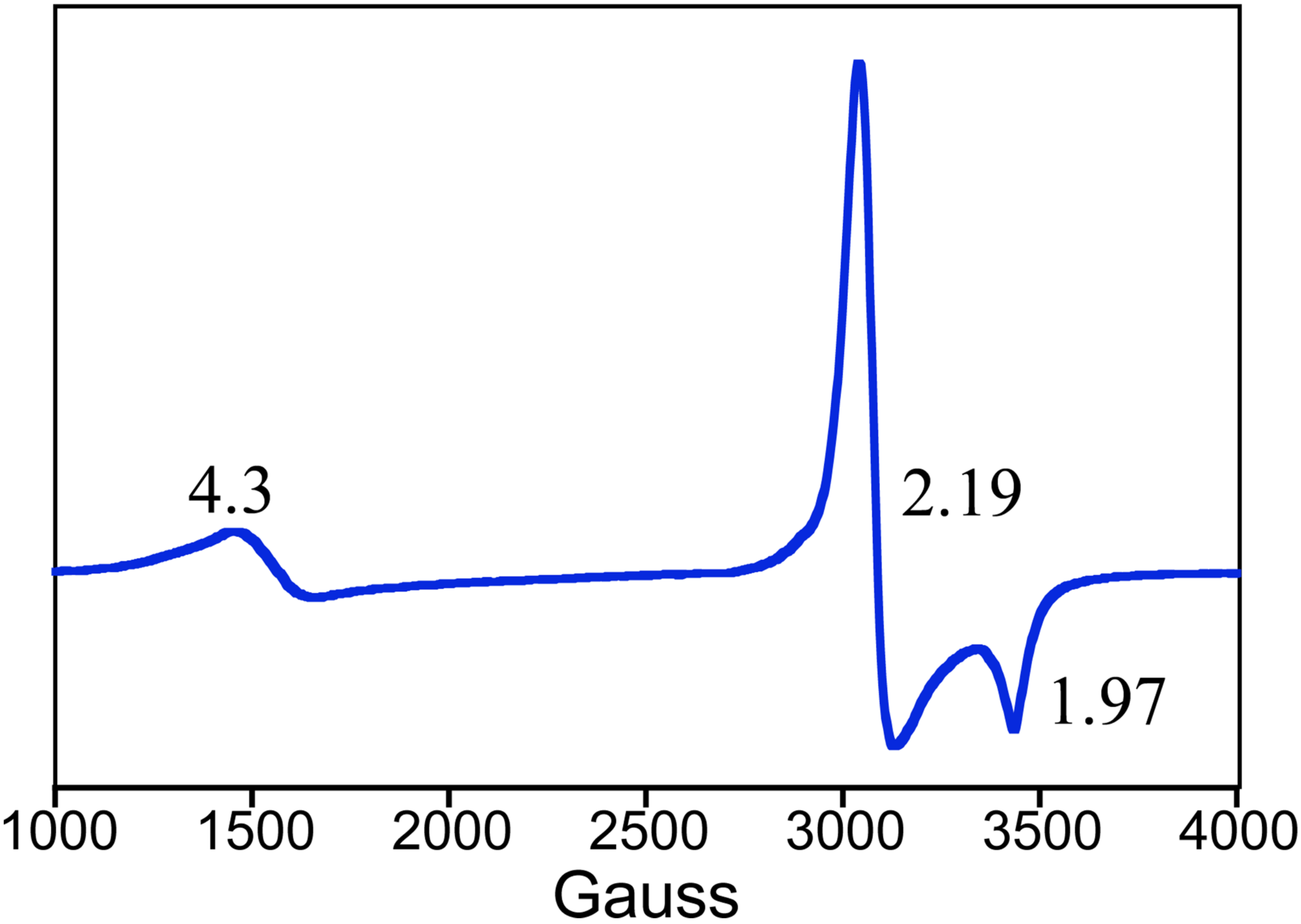

Figure 5.

9 GHz X-band EPR spectrum of $[Fe^{III}([15]aneN_4)(SC_6H_4p\text{-}Cl)(OO^tBu)]^+$ (**2a**) in CH_2Cl_2 at 15 K. Experimental conditions: Frequency, 9.475 GHz; microwave power, 2.012 mW; modulation frequency, 100.00 kHz; modulation amplitude, 10.00 G; receiver gain, 5.02 $\times 10^3$.

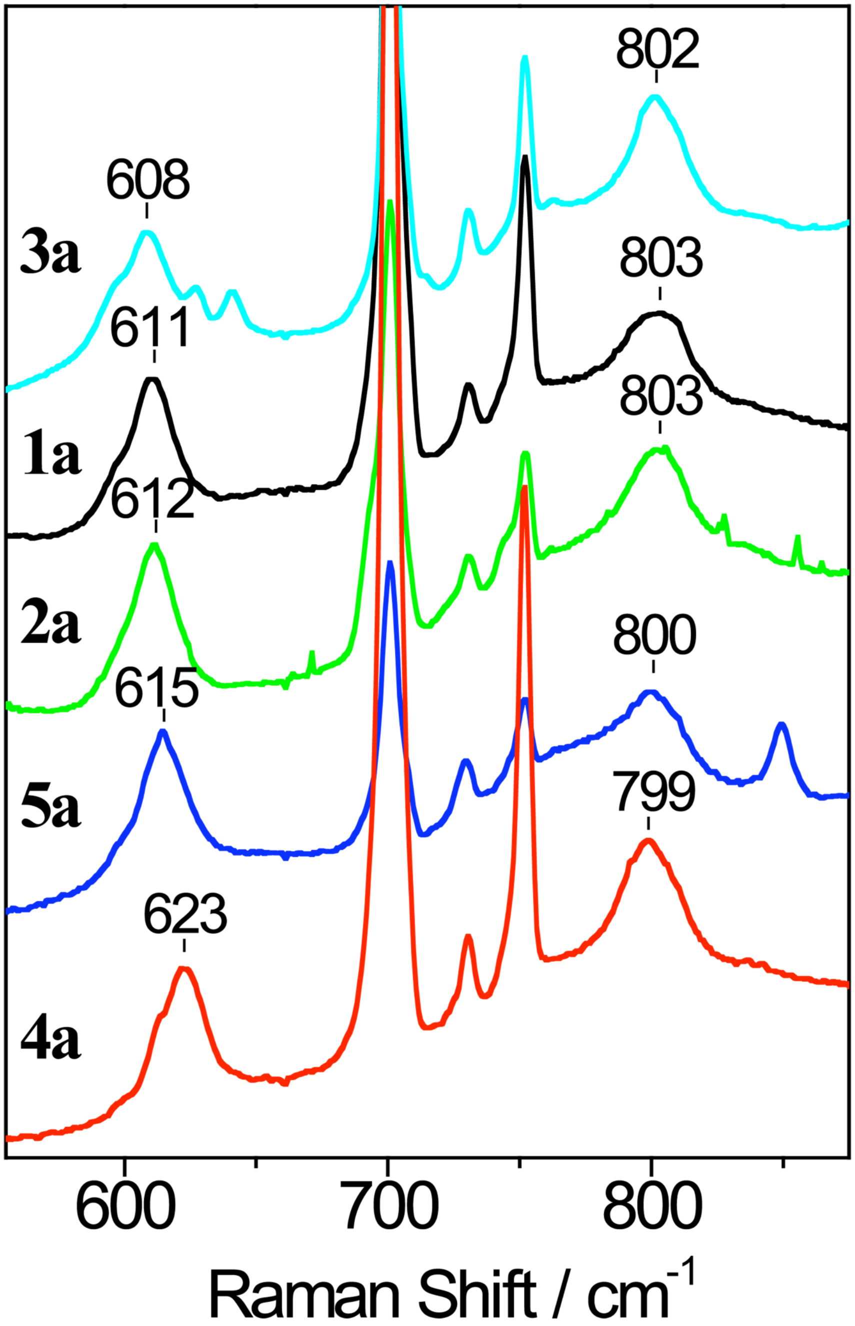

Figure 6.

Resonance Raman spectra of [Fe^{III}([15]aneN_4)(SAr)(OO^tBu)]$^+$ complexes **1a – 5a** in CH_2Cl_2 at 110 K obtained with 514-nm excitation. Intense Raman bands from the solvent are observed between 700 and 750 cm^{-1}. The 849-cm^{-1} band in **5a** is assigned to the NO_2 scissoring mode.

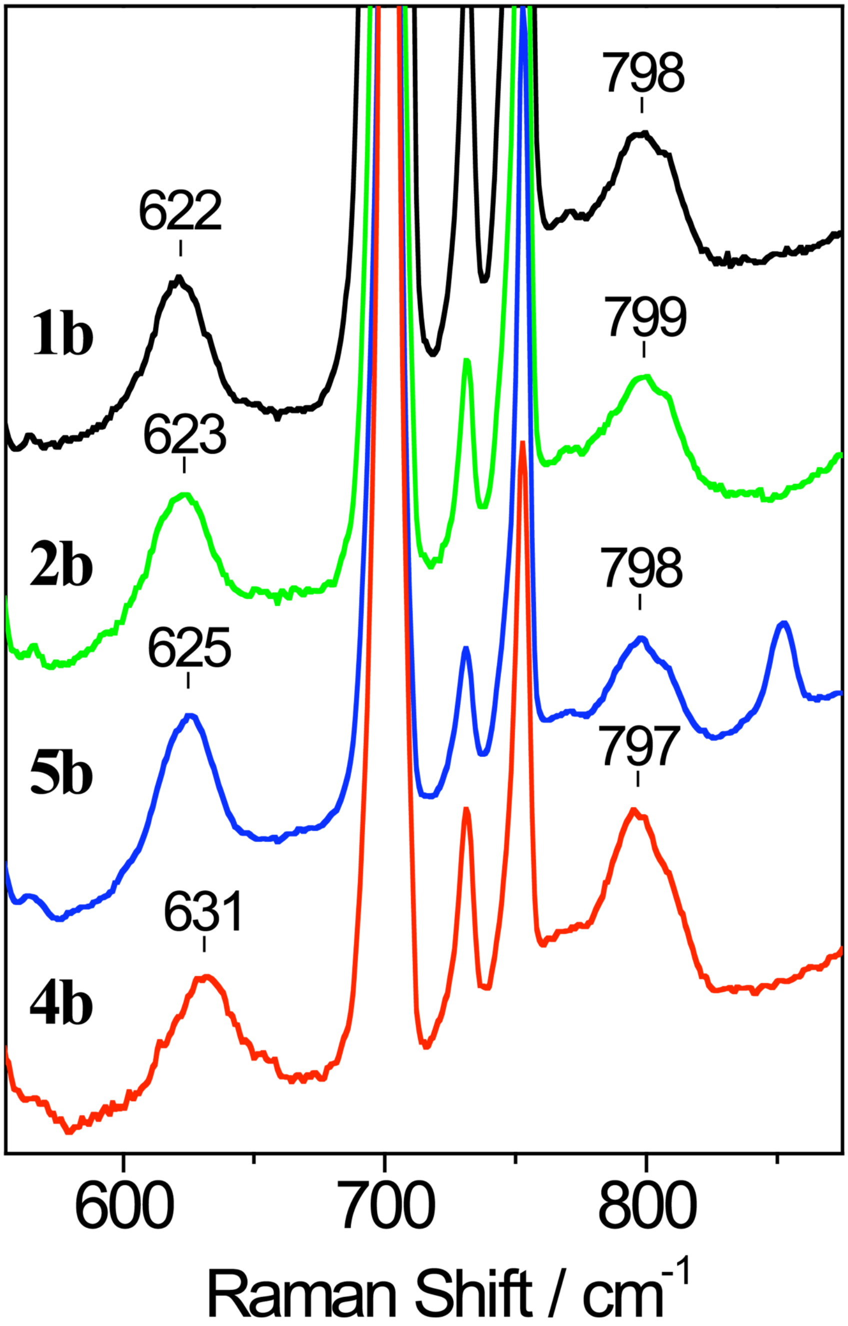

Figure 7.
Resonance Raman spectra of [Fe^{III}([15]aneN$_4$)(SAr)(OOCm)]$^+$ complexes **1b, 2b, 4b**, and **5b** (same experimental conditions as in Figure 6).

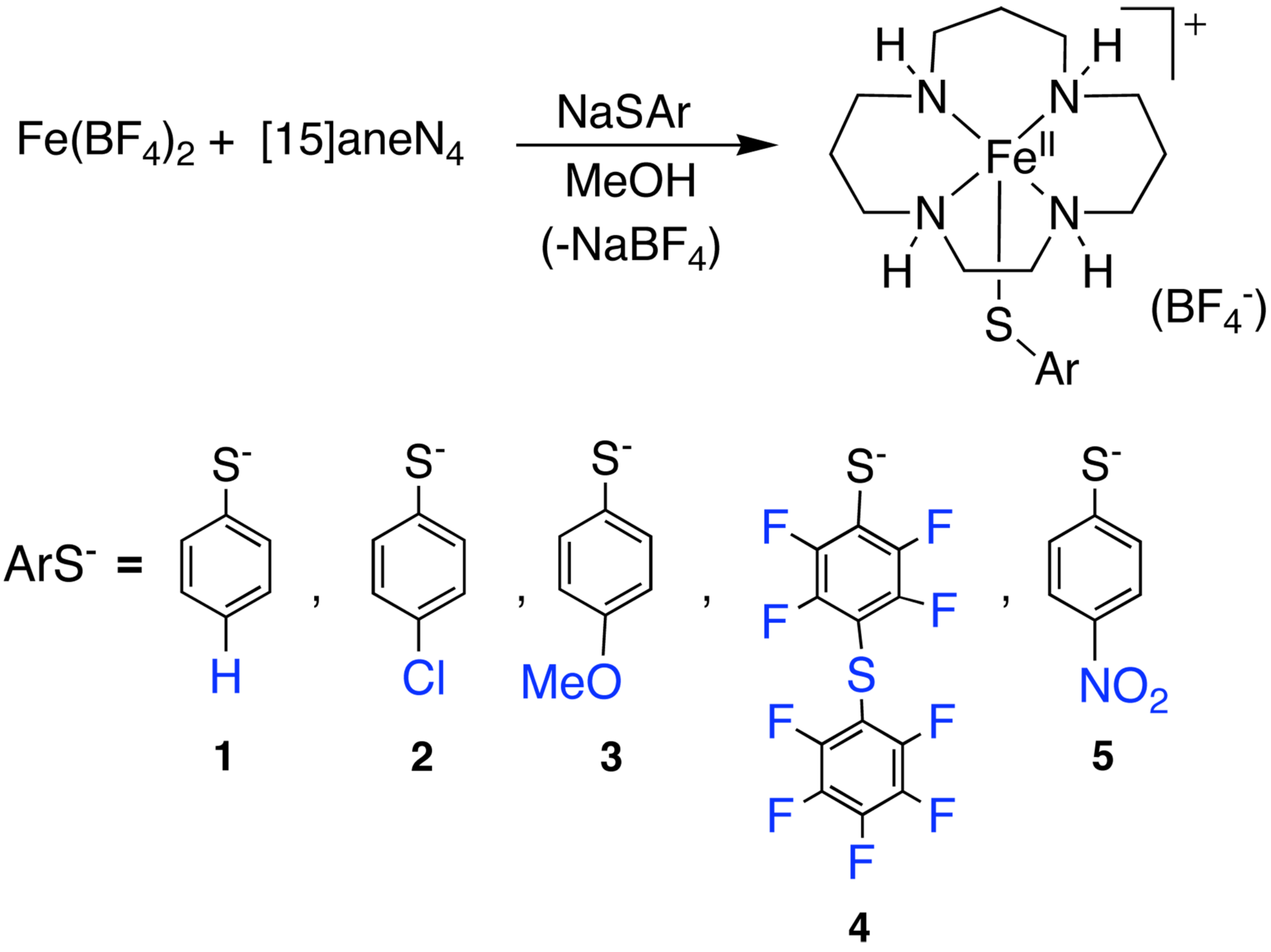

Scheme 1.

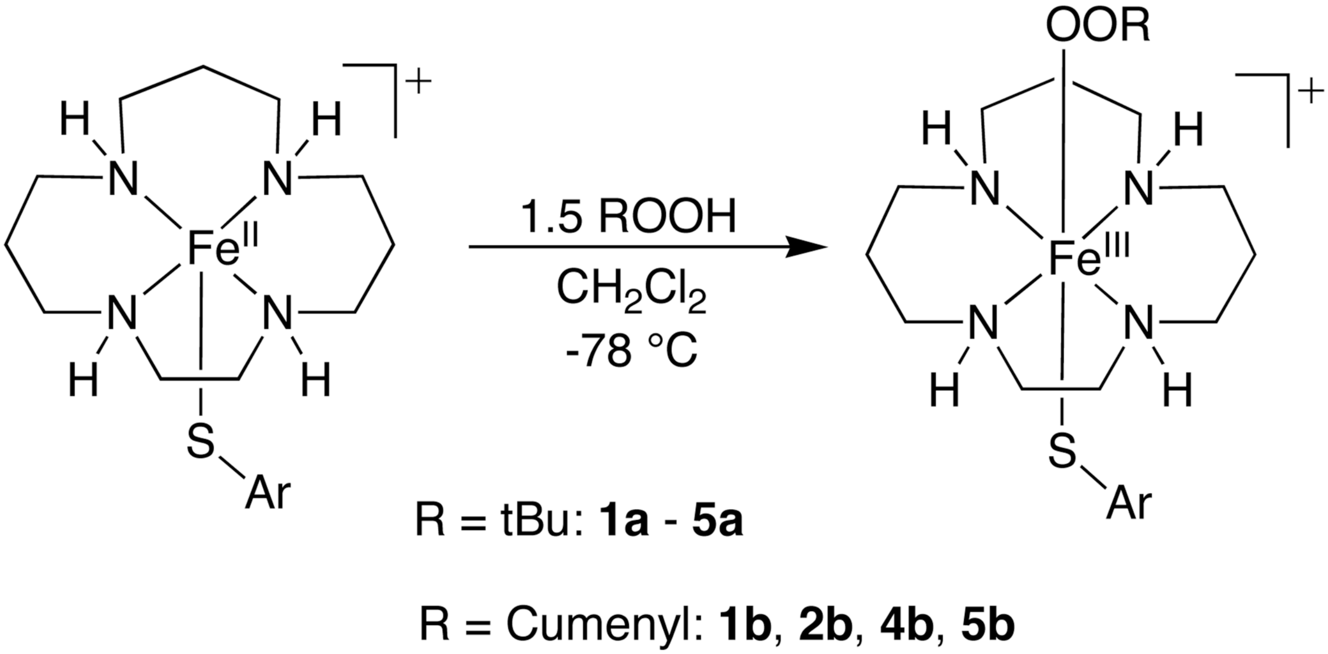
H
H
N
N
Fe^II
N
N
H
H
S
Ar
+
1.5 ROOH
CH2Cl2
-78 °C
OOR
H
H
N
N
Fe^III
N
N
H
H
S
Ar
+
R = tBu: 1a - 5a
R = Cumenyl: 1b, 2b, 4b, 5b

Scheme 2.

Table 1

Crystallographic Information for Complexes **1 – 5**

Parameter	**1**	**2**	**3**	**4**	**5**
Formula	$C_{17}H_{31}BF_4FeN_4S$	$C_{17}H_{30}BClF_4FeN_4S$	$C_{18}H_{33}BF_4FeN_4OS$	$C_{23}H_{26}BF_{13}FeN_4S_2$	$C_{17}H_{30}BF_4FeN_5O_2S$
M_r	466.18	500.62	496.20	736.26	511.18
cryst syst	monoclinic	Orthorhombic	Orthorhombic	monoclinic	orthorhombic
Space group	$P2_1/c$	$Pna2_1$	$Pna2_1$	Cc	$Pna2_1$
a (Å)	12.4027(7)	16.1010(4)	15.7595(4)	8.8233(2)	16.0267(3)
b (Å)	10.1280(6)	13.7952(4)	14.3395(3)	22.7707(6)	13.6455(3)
c (Å)	16.9164(11)	9.9077(3)	10.0194(3)	15.2423(4)	10.1189(2)
α (deg)	90	90	90	90	90
β (deg)	92.727(5)	90	90	103.444(3)	90
γ (deg)	90	90	90	90	90
V, Å^3	2122.5(2)	2200.66(11)	2264.22(10)	2978.46(13)	2212.93(8)
Z	4	4	4	4	4
Cryst color	colorless	colorless	colorless	colorless	dark red
T, K	110	110	110	110	110
R1 [$I > 2\sigma(I)$]	0.0707	0.0719	0.0947	0.0401	0.0831
GOF on F^2	1.253	1.071	1.076	1.047	1.080

Table 2

Relevant Bond Distances (Å) and Angles (deg) for Complexes **1 – 5**

Compd	**1**	**2**	**3**	**4**	**5**
Fe –N1	2.164(3)	2.206(7)	2.223(8)	2.161(3)	2.132(10)
Fe-N2	2.273(3)	2.251(8)	2.248(8)	2.250((3)	2.097(11)
Fe-N3	2.138(3)	2.075(7)	2.095(8)	2.088(3)	2.137(16)
Fe-N4	2.206(3)	2.160(7)	2.188(7)	2.229(3)	2.069(9)
Fe-S	2.3316(11)	2.3197(12)	2.3240(17)	2.3426(8)	2.3305(15)
N1-Fe-N2	79.45(12)	77.7(3)	77.8(3)	79.86(11)	72.3(6)
N1-Fe-N3	133.56(13)	133.4(3)	132.5(3)	132.06(12)	137.4(4)
N1-Fe-N4	85.98(12)	85.8(3)	84.9(3)	84.60(10)	86.4(6)
N2-Fe-N3	94.49(12)	96.0(3)	95.5(3)	95.78(12)	95.2(5)
N2-Fe-N4	163.08(13)	162.0(3)	161.0(3)	162.26(11)	153.2(8)
N3-Fe-N4	89.30(12)	90.1(3)	90.4(3)	88.28(12)	89.4(6)
S-Fe-N1	115.33(10)	109.4(2)	110.8(2)	107.85(8)	107.0(3)
S-Fe-N2	86.10(9)	96.6(2)	97.3(2)	100.04(9)	104.2(7)
S-Fe-N3	110.03(10)	117.2(2)	116.7(2)	119.83(9)	115.5(3)
S-Fe-N4	108.10(10)	95.59(17)	96.06(18)	92.79(8)	97.5(2)
Fe-S-C	116.90(12)	111.34(15)	111.3(4)[a] 106.0(5)[b]	112.29(10)	109.7 (6)[a] 110.3 (5)[b]
Fe-S-C(12)-C(13)	97.6(3)	−90.6(5)	−80.8(10)[a] −105.9(8)[b]	−132.8(2)	90.3(11)[a] 89.7(10)[b]
Fe-S-C(12)-C(17)	−87.5(3)	94.0(5)	102.2(12)[a] 82.7(13)[b]	52.0(3)	−92.9(14)[a] −92.7(11)[b]

[a] major component

[b] minor component

Table 3

Electrochemical Data for (N_4S(thiolate))Fe^{II} Complexes

Complex	E (mV) vs SHE (E_{pa} (mV) vs Ag/AgCl)	Solvent	ref
[Fe^{II}([15]aneN_4)(SC_6H_5)]BF_4 (**1**)	$706^{a,b}$ (501)	CH_2Cl_2	this work
[Fe^{II}([15]aneN_4)(SC_6H_4-*p*-Cl)]BF_4 (**2**)	$786^{a,b}$ (581)	CH_2Cl_2	this work
[Fe^{II}([15]aneN4)(SC6H4-*p*-OMe)]BF_4 (**3**)	$651^{a,b}$ (446)	CH_2Cl_2	this work
[Fe^{II}([15]aneN_4)(SC_6F_4-*p*-SC_6F_5]BF_4 (**4**)	$1018^{a,b}$(813)	CH_2Cl_2	this work
[Fe^{II}([15]aneN_4)(SC_6H_4-*p*-NO_2)]BF_4 (**5**)	$853^{a,b}$ (648)	CH_2Cl_2	this work
Fe^{II}[(Me_4-cyclam) (SC_6H_4-*p*-OMe)]OTf	$812^{a,c}$	CH_3CN	60
[Fe^{II}(L^8py_2)(SC_6H_4-*p*-CH_3)]BF_4	857^{c}	CH_3CN	59
[Fe^{II}(cyclam-PrS)]BPh_4	462^{c}	CH_3CN	36

[a] Anodic potentials for the irreversible oxidation wave.

[b] E versus SHE values were obtained by adding 205 mV to the recorded values versus Ag/AgCl.

[c] E versus SHE values were obtained by adding 242 mV to the reported literature values versus SCE.

Table 4

Vibrational Data Obtained from Resonance Raman Spectroscopy for Low-Spin Fe^{III}-OO^tBu Complexes

Low-spin Fe^{III}-OOtBu complex	υ (cm^{-1}) (Fe-O)	υ (cm^{-1}) (O-O)	*k*(Fe-O)[a] (mdyn/Å)	*k*(O-O)[a] (mdyn/ Å)	ref
$[Fe^{III}([15]aneN_4)(SC_6H_5)(OO^tBu)]^+$ (**1a**)	611	803	2.74	3.03	b
$[Fe^{III}([15]aneN_4)(SC_6H_4$-*p*-Cl)$(OO^tBu)]^+$ (**2a**)	612	803	2.75	3.03	b
$[Fe^{III}([15]aneN_4)(SC_6H_4$-*p*-OMe)$(OO^tBu)]^+$ (**3a**)	608	802	2.71	3.03	b
$[Fe^{III}([15]aneN_4)(SC_6H_4$-*p*-$NO_2)(OO^tBu)]^+$ (**5a**)	615	800	2.77	3.02	b
$[Fe^{III}([15]aneN_4)(SC_6F_4$-*p*-$SC_6F_5)(OO^tBu)]^+$ (**4a**)	623	799	2.85	3.01	b
$[Fe^{III}(TPA)(OH_n)(OO^tBu)]^{n+}$,[c]	696	796	3.53[d]	2.92[d]	29
$[Fe^{III}(TPA)(OO^tBu)(acetone)]^+$	693	788	3.52	2.93	26
$[Fe^{III}(5\text{-}Me_3\text{-}TPA)\ (OO^tBu)\ (acetone)]^+$	691	789	3.50	2.93	26
$[Fe^{III}(bpy)2(OO^tBu)(BzOH)]^{2+}$	678	808	3.37	3.08	30
$[Fe^{III}(b\text{-}BPMCN)(OO^tBu)(X)]^{2+}$,[e]	685	793	3.44	2.96	79
$[Fe^{III}(b\text{-}BPMCN)(OO^tBu)(X)]^{2+}$,[f]	680	789	3.39	2.93	79

[a] Force constants calculated for a diatomic oscillator using $\nu(cm^{-1}) = 1302.83[k(mdyn/Å)/\mu]^{1/2}$, where μ is the diatomic reduced mass, unless otherwise noted.

[b] This work.

[c] Recently reported as $[Fe^{III}(TPA)(OO^tBu)(NCMe)]^{n+}$ in the same solvent (CH_3CN).26

[d] Obtained from DFT calculations using a combined NCA/DFT approach.

[e] X = NCMe or H_2O.

[f] X= OTf or ROOH.